Ceilometer-Based Rain-Rate Estimation: A Case-Study Comparison With S-Band Radar and Disdrometer Retrievals in the Context of VORTEX-SE

Francesc Rocadenbosch^{ID}, *Senior Member, IEEE*, Rubén Barragán^{ID}, Stephen J. Frasier^{ID}, *Senior Member, IEEE*, Joseph Waldinger, David D. Turner^{ID}, Robin L. Tanamachi, and Daniel T. Dawson, II

Abstract—Attenuated backscatter measurements from a Vaisala CL31 ceilometer and a modified form of the well-known slope method are used to derive the ceilometer extinction profiles during rain events, restricted to rainfall rates (RRs) below approximately 10 mm/h. RR estimates from collocated S-band radar and portable disdrometer are used to derive the RR-to-extinction correlation models for the ceilometer–radar and ceilometer–disdrometer combinations. Data were collected during an intensive observation period of the Verification of the Origins of Rotation in Tornadoes Experiment Southeast (VORTEX-SE) conducted in northern Alabama. These models are used to estimate the RR from the ceilometer observations in similar situations that do not have collocated radar or the disdrometer. Such correlation models are, however, limited by the different temporal and spatial resolutions of the measured variables, measurement capabilities of the instruments, and the inherent assumption of a homogeneous atmosphere. An empirical method based on extinction and RR uncertainty scoring and covariance fitting are proposed to solve, in part, these limitations.

Index Terms—Atmospheric observation, geophysics, laser radar, lidar, meteorological radar, rainfall rate (RR).

Francesc Rocadenbosch and Rubén Barragán are with CommSensLab-UPC, Department of Signal Theory and Communications, Universitat Politècnica de Catalunya (BarcelonaTech—UPC), E-08034 Barcelona, Spain, and also with the Institute of Space Studies of Catalonia (IEEC), E-08034 Barcelona, Spain (e-mail: roca@tsc.upc.edu).

Stephen J. Frasier and Joseph Waldinger are with Microwave Remote Sensing Laboratory, University of Massachusetts, Amherst, MA 01003 USA.

David D. Turner is with the Global Systems Laboratory/Earth System Research Laboratories/NOAA, Boulder, CO 80305-3337 USA.

Robin L. Tanamachi and Daniel T. Dawson, II are with the Department of Earth, Atmospheric, and Planetary Sciences, Purdue University, West Lafayette, IN 47907 USA.

I. INTRODUCTION

THE first Verification of the Origins of Rotation in Tornadoes EXperiment-Southeast (VORTEX-SE) [1] field campaign took place during March and April 2016 around Belle Mina, AL, USA (34.6902° N, −86.8845° E). During this experiment, the University of Massachusetts Microwave Remote Sensing Laboratory (UMASS MIRSL), Amherst, MA, USA, and Purdue University, West Lafayette, IN, USA, deployed a mobile S-band frequency-modulated continuous-wave (FMCW) radar operating at 2.94 GHz, a near-infrared Vaisala CL-31 lidar ceilometer, and an OTT Parsivel2 disdrometer with the aim to study the spatial and temporal evolution of liquid water clouds and moderate rain events during 2 months of continuous measurements [2]. The National Oceanic and Atmospheric Administration (NOAA) National Severe Storms Laboratory, Norman, OK, USA, deployed a Doppler lidar nearby as part of their Collaborative Lower Atmosphere Mobile Profiling System (CLAMPS) atmospheric profiling system [3].

A key parameter in precipitation studies is the rainfall rate (RR), which is defined as the depth of accumulated liquid precipitation over a unit area of the surface per unit time. One factor that influences the retrieved RR is the assumed form of the drop size distribution (DSD) (see [4]–[8]), and—subsidiary to it—the median drop diameter, which is related to the shape of the drops and the processes of coalescence and breakup [9]. The assumed DSD modulates characteristics such as the growth, diameter, and lifetime of raindrops, as well as microphysical processes such as the evaporation rates of precipitation particles and the rate at which raindrops fall through different atmospheric layers [10], [11].

Disdrometers and radars [12]–[14] have successfully been used to study the variability of rain and liquid water content. S-band radars are mostly unaffected by attenuation resulting from precipitation [15]. Disdrometers measure the rainfall intensity, DSD, and fall velocity precisely, and they sample with a specified temporal resolution (e.g., 10 s) [16]. Concerning costs, the cost of a ceilometer is around U.S. $ 30 000, a microrain radar is approximately between U.S. $ 35 000 and 100 000 depending on the automation/stand-alone capabilities included, whereas an S-band radar profiler is about U.S. $ 35 000. A disdrometer costs between U.S. $5000–6000.

These instruments, however, have their limitations. On one hand, disdrometers cannot provide, in a direct way, information about the vertical variations in characteristics of the rain. In addition, measurements can be prone to large errors in situations with exceptionally small raindrops (less than 1 mm diameter) during intervals with a small number of raindrops [17]. On the other hand, vertically pointing S-band radars have difficulty providing reliable information of the vertical distribution of rain close to ground level because of near-field and/or parallax effects.

Although ceilometers were primarily designed to be autonomous instruments capable of determining the cloud height at high temporal resolution, they offer attractive possibilities for rain detection when used with collocated equipment in a synergistic manner. Ceilometer technology today also enables the detection of boundary-layer aerosol content [18]. Mono-axial ceilometers typically have a much lower height of the laser-telescope crossover function (typically below 100 m) [19], thereby allowing profiling very near the surface, and they maintain a good signal-to-noise ratio (SNR) in light rain or even in the absence of rain. As with any active profiling system, the ceilometer return signal is affected by the number and type of raindrops and the extinction between the scatterer and the receiver.

Historically, rain measurements at optical wavelengths preceded the use of lidars and were based on optical transmissometers and Mie-scattering classical theory [20]; these early studies used size-distribution models for rain and fog droplets [4]. Rensch and Long [21] combined these models with transmission measurements at 0.63 and 10.6 μm and related optical extinction and backscatter coefficients to rain intensities. Pruppacher and Beard [22] also studied the shape of drops falling at terminal velocity by means of a wind tunnel, where the terminal velocity depends strongly on the diameter of the raindrop. According to [21] and [23], a key assumption to using the correlation between the RR and the atmospheric optical extinction derived from fixed-orientation ceilometer measurements (RR-to-extinction models; hereafter, RR–α models) is that droplets maintain symmetry in the direction of fall (i.e., assumption of small (spherical) drops and no canting [10, p. 249]). Otherwise, geometric optics calculations of light scattering by nonspherical raindrops reveal a strong dependence on the phase matrix that invalidate ceilometer measurements [24], [25]. More recently, Roy and Bissonnette [26] showed that rain extinction coefficients and depolarization ratios varied strongly depending on the lidar zenith angle (0–75°), demonstrating the importance of performing measurements with constant lidar scan direction. Although they showed that single-wavelength lidar measurements could not be used to infer raindrop deformations and size directly, they also stressed the need to couple the lidar with complementary sensors (e.g., Doppler radar or *in situ* rain gauges like the disdrometer) for more precise description of raindrop dynamics.

To our knowledge, Lewandowski *et al.* [27] made the first empirical effort to observe the small-scale spatial and temporal evolution of precipitation over a small sampling area (1–2-km measurement line) by means of lidar. They used a 25-mJ energy, 50-Hz pulse repetition rate, 1064-nm wavelength, 25-m aperture lidar in a horizontal configuration to correlate the disdrometer-measured RR with the lidar-measured optical extinction (RR–α relationship). They assumed a Marshall–Palmer (MP) DSD, and molecular (Rayleigh) and aerosol (Mie) background extinction contributions were neglected between the instrument and the rain location for RR values between 0.1 and 100 mm/h.

In this work, RRs are inferred from observations by a vertically pointed ceilometer and compared with co-located S-band radar and disdrometer RR measurements. This work aims to complement the studies of [27] and the contributors above by addressing three goals: 1) to demonstrate the feasibility of using a vertically pointed ceilometer to measure low-to-moderate RRs (0.5–9 mm/h); 2) to extend the applications of a widely used lidar inversion algorithm (the slope method, [28]) to these comparatively low RRs and investigate the impacts of the assumptions made in the method; and 3) to establish the RR–α dependence for the ceilometer–radar and ceilometer–disdrometer combinations. The latter goal is achieved by applying an appropriate fitting procedure that accounts for the inherent intercomparison uncertainty among the RR measured by these three different instruments. For example, while the ceilometer optical extinction—as estimated by the slope method—is the column average over a predefined height interval, the radar RR is an estimate at a reference height, and the disdrometer RR is a ground-level measurement.

This article is organized as follows: Section II describes the instrumentation and preprocessing techniques used by giving an overview of a first rain episode. Section III addresses the retrieval methods used: Section III-A and the Appendix describe the radar RR and reflectivity factor retrieval procedures, Section III-B deals with ceilometer-based slope-method retrieval of the average extinction coefficient, and Section III-C formulates the error treatment associated with the RR and rain extinction estimates. Section IV describes the meteorological conditions during the VORTEX-SE rain episode, derives the RR–α model to estimate the RR from extinction measurements, and discusses the uncertainties. Section V tackles an additional case study with a view toward model verification, and Section VI gives concluding remarks.

II. INSTRUMENTS AND DATA PREPROCESSING

A. Instruments

The four principal instruments used in this study were operated as part of the VORTEX-SE 2016 field campaign [29]. The characteristics of the four instruments used are summarized in Table I. The truck-mounted ceilometer and the S-band radar operated together from March 11, 2016, to May 1, 2016. The portable disdrometer [30] was collocated with these instruments from April 27, 2016, to May 1, 2016, only. The Doppler lidar was installed approximately 100 m to the west of the radar/ceilometer setup. All remote sensing instruments were pointing vertically so that the range and height are interchangeable.

The Vaisala CL-31 lidar ceilometer [31] operates at 910-nm wavelength with 1.2-μJ pulse energy, 8192-Hz pulse repetition

TABLE I
MAIN SPECIFICATIONS OF THE INSTRUMENTS

Instrument	λ	Pointing	Measured parameter	Raw spatial resol.	Raw temporal resol.
Ceilometer	910 nm	Vertical (0.1 deg FOV)	Attenuated backscatter (uncal.)	10 m	16 s
S-band Radar	15 cm	Vertical (3 deg HPBW)	Volume reflectivity [m^{-1}]	5 m	1 s
Disdrometer	780 nm	Horizontal, In-Situ	Rainfall rate [mm/h]	54 cm^2 (sampling area)	10 s
Doppler lidar	1540 nm	Vertical	Vertical velocity [m/s], CNR [dB]	100 m	1 s

FOV: Field Of View (angle is full width), *HPBW:* Half Power Beam-Width, *CNR:* Carrier-to-Noise Ratio. λ: Wavelength.

rate, and mono-axial arrangement (i.e., the optical axis of the emission laser and receiving telescope coincide). The latter enables a starting range of full overlap of about 70 m, which determines the minimum usable range. The ceilometer gives the profile of the attenuated atmospheric backscatter; however, as it lacks absolute calibration [32], herein this variable is simply referred to as the "range-corrected lidar signal." The atmospheric molecular return cannot be measured as it falls below the ceilometer noise level [19].

The S-band FMCW radar [33], collocated with the ceilometer, uses a pair of 2.4-m-diameter parabolic antennas each with 34-dB gain. This radar provides vertical profiles of the reflectivity factor (from the measured volume spectral reflectivity), vertical velocity, and spectrum width at 5-m vertical resolution (Table I). The S-band radar can detect both precipitation and clear-air echo [34], [35], thereby enabling studies of both precipitation and the evolution of the atmospheric boundary layer. The use of separate antennas for transmission and reception results in a reduction in reflectivity below 300 m height (i.e., measurements made in the lowest 300 m are not well-calibrated). In addition, in cases of low RR (<0.5 mm/h), radar data can be noise corrupted; RRs below this threshold are not considered reliable [36], [37]. As with the ceilometer, this instrument operated continuously during the VORTEX-SE campaign and provided vertical atmospheric profiles. Both instruments were collocated on the same vehicle and vertically aligned so as to provide information representative of the same vertical column of the atmosphere.

The OTT Parsivel Disdrometer [38], [39] is part of the Portable *In situ* Precipitation Station (PIPS) developed jointly by Purdue University and the U.S. National Severe Storms Laboratory [30]. A disdrometer is an *in situ*, ground-based, 1-D optical instrument which provides precipitation size data on a particle-by-particle basis. An infrared laser illuminates a linear array of photodiodes (measurement area). When falling precipitation particles cross the measurement area, they cause variations to the photodiodes' signal. These variations depend

on the diameter of the drops and their fall velocity, producing an inferred DSD from which the RR is derived.

Finally, the Leosphere Windcube 100S [40] is a 1.54-μm wavelength, conically scanning lidar that uses the Doppler effect combined with the velocity-azimuth display (VAD) algorithm [41], [42] to generate vertical wind profiles up to typically 3 km in height (100-m resolution, 1-s accumulation time). The Doppler lidar was mainly used to confirm the presence of rain through time and height-resolved profiles of the vertical velocity and carrier-to-noise ratio (CNR).

B. Event Overview and Preprocessing Methods

Among the 54 days of observation, only two correspond to substantially rainy days (time-continuous rain curtain over 2 h), March 31 and April 29–30 (overnight). The latter event is the most useful to study because the portable disdrometer was co-located with the radar and the ceilometer that day. Fig. 1 shows an overview of the April 29–30, 2016, rain event (22:00–02:00 UTC). Fig. 1(a)–(d) qualitatively shows that the rain event begins around 22:30 UTC, reaches peak intensity at the middle of the period (22:30–00:30 UTC), and then gets progressively weaker with time before ending at 01:15 UTC.

Because of the different raw temporal resolutions among the radar, the ceilometer, and the disdrometer (Fig. 1), the measurement time series from these instruments were resampled to a common master-time resolution, $\Delta T_{\text{master}} = 16$ s. In addition, the analysis was restricted to altitudes at and below 3 km to avoid the melting layer at approximately 3.3-km above ground level (AGL).

The ceilometer attenuated backscatter profiles were smoothed temporally and spatially before deriving the extinction coefficient using the slope method (Section III-B). The ceilometer measurements have been further time-averaged to a temporal resolution, $\Delta T_{\text{clean}}^{\text{ceilo}} = 80$ s (hereafter, the smoothed temporal resolution or time bin, ΔT) and a smoothed spatial resolution, $\Delta R_{\text{clean}}^{\text{ceilo}} = 0.2$ km. A low-pass finite impulse response (FIR) digital filter [order = 50, cutoff frequency = 0.1 (Nyquist-normalized)] has been used. The filter uses a Hamming-window-based design to achieve high noise rejection and linear phase [43].

These smoothed resolutions provide mean SNRs of 19 and 14 dB at $h_1 = 0.5$ km and $h_2 = 2$ km, respectively. These are typical starting and end ranges (heights) of the slope-method processing interval (Section III-B). The SNR levels given in Section II-B ensure a virtually noiseless log-range-corrected signal, $G(h)$, over the whole processing range [44]. The noise variance has been estimated according to the procedure described in [45]. In Section III, the temporal resolution of the retrieval products (rainfall rate, RR, and rain extinction coefficient, α) is one time bin (80 s).

III. RETRIEVAL METHODS

A. Radar Case

The S-band FMCW radar signal processing proceeds as follows: the radar transmits a linear frequency-modulated signal over a short interval, typically a few milliseconds. Radar echoes are mixed with a copy of the transmitted signal and
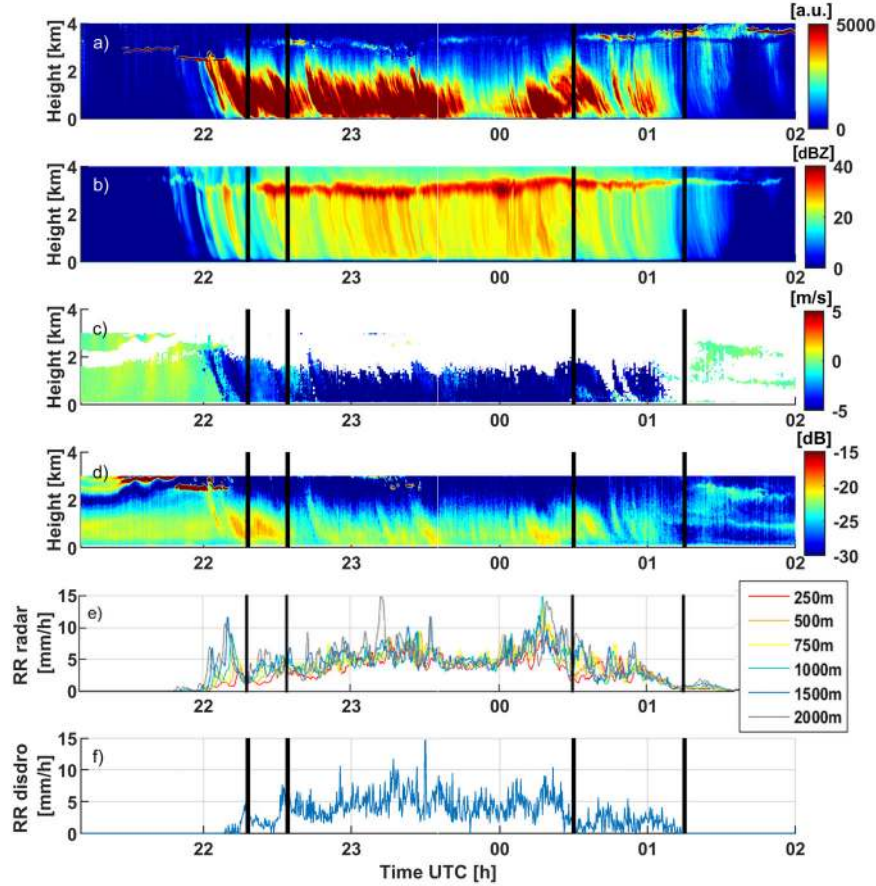
Fig. 1. Overview of April 29–30, 2016, rain episode. (a) Ceilometer range-corrected lidar signal (arbitrary units, [a.u.]) versus time. (b) Radar reflectivity factor [dBZ] computed after (22). (c) Doppler lidar vertical velocity [m/s]. Velocities associated with a CNR < −26 dB are not plotted. (d) Doppler lidar CNR [dB]. (e) RR [mm/h] time series measured by the radar at different heights, from 250 up to 2000 m. (f) RR [mm/h] time series measured by the disdrometer. Vertical black lines (a)–(f) delimit the time intervals discussed in Section IV-A. Temporal resolution (a)–(f) is 16 s. Spatial (height) resolution (a)–(f), see Table I.

low-pass filtered yielding a beat frequency that indicates the range of the target. All targets are sorted in range by applying a Fourier transform to the recorded echo data. Following this process, the resulting complex (in-phase and quadrature) samples can be treated like any pulsed radar echo. Doppler spectra are computed in normal fashion by applying a Fourier transform to the time series of echoes at each range over a given time interval. The Doppler spectra may be represented either versus Doppler frequency or versus radial (vertical) velocity, given the relationship between the two

$$v_n = n\Delta v = f_n \frac{\lambda}{2} \tag{1}$$

where $n = 1 \ldots N$ ($N = 64$) is the index of the Doppler spectrum, Δv is the velocity resolution ($\Delta v = \Delta f \lambda/2$), λ is the radar wavelength (15 cm; Table I), and, $f_n = n_i \Delta f$ is the discrete frequency, with i the range index ($i = 1 \ldots I$, $I = 32$ gates) and Δf the frequency resolution of the Doppler spectrum (190.735 Hz).

The steps to estimate the radar reflectivity factor (Z) and RR as a function of height are described in detail in the Appendix. Briefly, a DSD is obtained from the Doppler spectrum through a change in variable assuming that the drops are Rayleigh

scatterers that fall at their terminal velocities, thus establishing a relationship between velocity and size. Vertical air motion (updrafts or downdrafts) will affect the velocity inducing an error in size if not compensated. Given a DSD, denoted as $N(D)$, the reflectivity factor can be computed as follows:

$$Z = \int_0^\infty N(D)D^6 dD \tag{2}$$

which is the sixth moment of the DSD, while the RR depends on the drop volume (third moment) and fall velocity

$$RR = \frac{\pi}{6} \int_0^\infty N(D)D^3 v(D) dD. \tag{3}$$

Fig. 2 provides a computation example at a reference height of 1000 m. The example departs from the 1-h time-average measured reflectivity density with respect to the velocity after the vertical air-motion correction was applied to ensure that the clear-air echo (left panel, red strip) is at 0 m/s. In the central panel, the reflectivity factor, Z, is computed by plotting the reflectivity density at the reference height scaled by the factor $(\lambda^4/\pi^5)(1/|K_w|^2)$ and by finding the area under the curve [see (22)]. Fig. 2(c) shows the DSD, $N(D)$, as well as the integrand kernels $N(D)D^3$ and $N(D)D^6$ used in (3) and
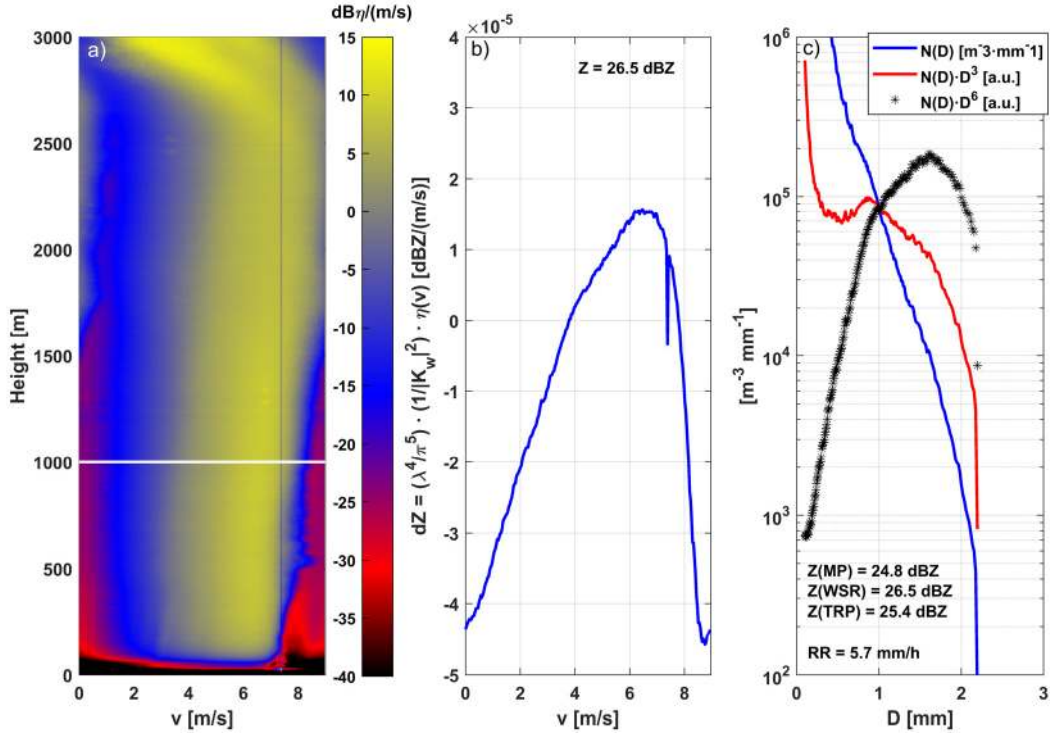
Fig. 2.   Computed radar data products at 1000-m reference height (case 1, April 30, 2016, 00:00–01:00 UTC, vertical air-motion correction 2 m/s [46]). (a) Volume reflectivity density with respect to the velocity as a function of height, $\eta(v)$ $[dB\eta/(\text{m/s})]$ (see (15), $dB\eta = 10\log\eta$). The white horizontal line indicates the reference height (1000 m). (b) Reflectivity factor density $dZ = (\lambda^4/\pi^5)(1/|K_w|^2)\eta(v)$ $[dB\eta/(\text{m/s})]$ with respect to the velocity (equivalently, (22) using that $\eta = \int_0^\infty \eta(v)dv$). The label shows the reflectivity factor [dBZ] computed as the area under the curve. (c) (blue trace) Drop size distribution [drops/$(\text{m}^3 \cdot \text{mm})$]; (red trace) RR integrand term $N(D)D^3$[a.u.] [see (3)]; (black dashed trace) reflectivity-factor integrand $N(D)D^6$ [a.u.] [see (2)] as a function of velocity [see (19)]. MP, WSR, and TRP stand for the different Z–RR models considered (see text).

(2) above to compute the RR and the radar reflectivity factor, respectively, from the DSD. The results are quality-assured by comparing the reflectivity factor obtained after (22) [26.5 dBZ, area under the curve, Fig. 2(b)] to the reflectivity factor estimated from the RR obtained after (3) [5.7 mm/h, Fig. 2(c)] through the WSR-88D default model, $Z = 300(\text{RR})^{1.4}$ [47]. This WSR model gives 26.5 dBZ in perfect coincidence. The MP relationship, $Z = 200(\text{RR})^{1.6}$ [4], and the WSR-88D tropical relationship, $Z = 250(\text{RR})^{1.2}$ (TRP), have also been considered with slightly poorer agreement (25.4 and 24.8 dBZ, respectively).

B. Ceilometer Case: Extinction Coefficient Retrieval

Because the ceilometer operates at 910-nm wavelength (near infrared), the molecular backscattering cross section is very small and because the ceilometer is a low-energy aperture product lidar, the molecular backscatter cannot be measured [19]. As a result, range-resolved inversion methods like the Klett–Fernald's algorithm [48]–[50] cannot be used. Alternatively, the selected method to estimate the optical extinction coefficient from the ceilometer is an adapted version of the classic slope method [28]. The slope method is based on the single-scattering monostatic lidar equation in differential form [51]

$$\frac{dG(h)}{dh} = \frac{1}{\beta(h)}\frac{d\beta(h)}{dh} - 2\alpha(h) \qquad (4)$$

where $G(h)$ is the logarithm of the measured range-corrected lidar signal $(\ln[P(h)h^2])$, $\alpha(h)$ is the total atmospheric extinction coefficient profile, $\beta(h)$ is the total backscatter coefficient profile, and h is the range (height). The slope method assumes a homogeneous stratified atmosphere along the lidar's observing path—the most limiting assumption of the method—and allows to estimate the average atmospheric extinction based on linear regression analysis applied to the logarithm of the range-corrected lidar signal

$$G(h) = \ln[P(h)h^2] = \ln K\beta - 2\alpha h \qquad (5)$$

where K is the ceilometer instrument constant (unknown) and where the homogeneity approximation $\alpha(h) \approx \alpha$, $\beta(h) \approx \beta$ has been used. Because the 910-nm molecular backscattering cross section is negligible, the total extinction coefficient is equal to the aerosol extinction coefficient ($\alpha \approx \alpha_{\text{aer}}$).

Under ideal noiseless conditions, when a linear fit of the form $y = mh + n, h \in [h_1, h_2]$ is applied to (5), the estimated slope and intercept are $\hat{m} = -2\alpha$ and $\hat{n} = \ln K\beta$, respectively. Therefore, the average extinction coefficient in the range interval $I = [h_1, h_2]$ is retrieved as minus one half of the logarithm of the range-corrected lidar signal, $G(h)$.

Fig. 3 illustrates the logarithm of 132 range-corrected ceilometer signals versus height during a rain measurement (Fig. 3(a), 22:19 to 01:15 UTC) and two nonrain measurements [Fig. 3(b)], one just before the start of the rain event (21:36 to 21:40 UTC) and one after (01:41 to 01:45 UTC).

event (Section IV). Purple and green traces inside the hatched areas represent the background extinction coefficient, $\alpha_{\text{no\_rain}}$, before (21:36–21:40 UTC) and after (01:41–01:45 UTC) the rain episode, respectively. The hatched areas delimit the corresponding upper and lower background extinction error bars. Time resolution is one bin (80 s), and spatial resolution is 200 m.

The estimated slopes from the logarithm of the range-corrected power are greater in Fig. 3(a) (rain measurement) than in Fig. 3(b) (nonrain). This is because during the rain measurement the ceilometer signal undergoes extinction due to aerosols and raindrops

$$\alpha = \alpha_{\text{aer}} + \alpha_{\text{rain}} \quad (6)$$

while during nonrain measurements the total extinction is only due to aerosols ($\alpha_{\text{no\_rain}}$) [see Fig. 3(c)].

Under the approximation that the aerosol background with and without rain is similar ($\alpha_{\text{aer}} \approx \alpha_{\text{aer}}^{\text{no\_rain}}$), the rain extinction is estimated as the differential extinction

$$\alpha_{\text{rain}} = \alpha - \alpha_{\text{no\_rain}}. \quad (7)$$

This approximation essentially requires closely time-spaced rain/no-rain measurements, and an assumption is made that the rain even does not significantly reduce the aerosol load through scavenging.

1) Selection of the Starting and End Processing Ranges of the Slope Method: Selection of starting and end height ranges, h_1 and h_2, respectively, is not easy because inhomogeneities encountered in the profile of $D(h)$ with height break the homogeneity assumption inherent to the slope method. Selection of height ranges h_1 and h_2 combines different requirements: A minimum height of 0.3 km is required for starting height h_1 to ensure that this height is greater than the spatial resolution of the smoothing spatial filter used ($\Delta R_{\text{clean}}^{\text{ceilo}} = 0.2$ km, Section II-B) and, therefore, free from initial filter transients. The maximum height allowed for h_2 is 2.8 km to be well below the melting layer [Fig. 1(b)]. This maximum height is often further limited by the proximity of notches in the profile of $D(h)$ [Fig. 3(a) and (b)]. These notches are caused by negative measurement noise spikes which, when combined with low backscattered power levels, translate into singularities in the logarithm of the range-corrected power [i.e., $P(h)$ negative in (5)]. By experiment, a minimum distance between h_1 and h_2 of 0.6 km ($3\Delta R_{\text{clean}}^{\text{ceilo}}$) is also necessary so that the slope-method linear fit averages out the residual oscillatory overshoot caused by the smoothing filter. Selection of height ranges h_1 and h_2 has been done in semisupervised fashion departing from an initial guess $[h_1, h_2] = [0.7, 2.0]$ km and by trying to attain the lowest relative root-mean-square error (RMSE) in each retrieval case upon manual small perturbation of the initial guess. In what follows, the starting and end height ranges used will be denoted by the range interval $I = [h_1, h_2]$.

Formally, the relative RMSE of the retrieved total extinction coefficient is defined as follows:

$$\text{RMSE}_{\alpha,\text{rel}} = \frac{\text{RMSE}_\alpha}{\alpha} \quad (8)$$

where RMSE_α is the absolute RMSE on the total extinction coefficient (in what follows, "the extinction RMSE") estimated
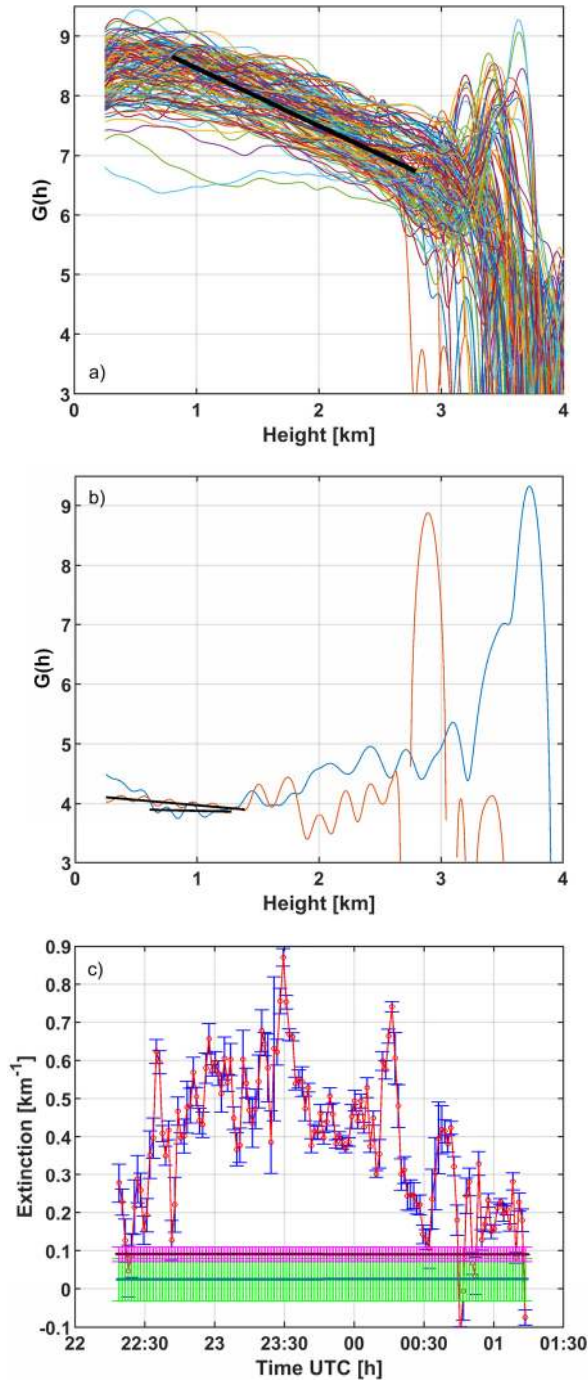

Fig. 3. Slope-method results (Belle Mina, April 29–30, 2016, 21:36–01:45 UTC). (a) Logarithm of the range-corrected ceilometer signals, $G(h)$, during the rain interval. (b) Logarithm of the range-corrected background signal, $G(h)$, before the start of the rain episode (orange trace) and after ending (blue trace). (c) Total extinction coefficients (red circles), α [see (6)], with error bars (blue), derived from the rain profiles of (a) by means of the slope method (see text).

Solid lines between 300 and 1400 m and between 600 and 1300 m represent the linear fits used to, respectively, derive the background total extinction coefficients ($\alpha_{\text{before}}^{\alpha\_\text{no\_rain}} = 0.09 \pm 0.02$ km^{-1}, $I_{\text{before}} = [0.3, 1.4]$ km; $\alpha_{\text{after}}^{\alpha\_\text{no\_rain}} = 0.02 \pm 0.05$ km^{-1}, $I_{\text{after}} = [0.6, 1.3]$ km). Fig. 3(c) summarizes the retrieved total extinction coefficient for the whole rain

TABLE II
Time and Height Intervals Associated With Minimum Relative RMSE [See (8)] When Applying the Slope Method to the Ceilometer Profiles of Fig. 3(a) and (b)

CATEGORY	Time Interval	Slope-Method Height Interval
Rain profile (Fig. 3a)	22:19 - 22:34 UTC	$I_1 = [0.3, 1.8]$ km
	22:34 - 00:29 UTC	$I_2 = [0.8, 2.8]$ km
	00:29 - 01:15 UTC	$I_3 = [0.5, 2.4]$ km
Background-extinction profile (Fig. 3b)	21:36 - 21:40 UTC	$I_{before} = [0.3, 1.4]$ km
	01:41 - 01:45 UTC	$I_{after} = [0.6, 1.3]$ km

as follows:

$$\text{RMSE}_\alpha = \frac{1}{2} \frac{\text{RMSE}_y}{h_2 - h_1} \tag{9}$$

where RMSE_y is the RMSE of linear regression over the measurements, $y_i = D(h_i)$, $i = 1, \dots, N$. The term $\text{RMSE}_m = \text{RMSE}_y / (h_2 - h_1)$ in (9) above estimates the RMSE on the retrieved slope. Factor 2 accounts for the fact that extinction is retrieved as minus one half of the estimated slope because of the two-way traveling path of the laser beam. Hence, the incurred error is also one half of the RMSE on the retrieved slope. Table II summarizes the condition of minimum relative RMSE, $\text{RMSE}_{\alpha,\text{rel}}^{\text{rain}}$ (see (8)), in different time intervals of the rainy profiles of Fig. 3(a), and when estimating the background extinction profiles before and after the start of the rain episode [see Fig. 3(b)].

C. RR-to-Extinction Intercomparison: Error Treatment

In this section, we limit the error treatment to the random error associated with the mean RR estimated from the radar/disdrometer combination (Section III-A) and to the rain extinction coefficient derived from the slope method using ceilometer measurements of total and background atmospheric extinction [Section III-B, (7)]. As mentioned in Section II-B, these products are retrieved with a temporal resolution of 80 s. In Sections IV-B and V, the estimated extinction coefficient will be related to the retrieved RRs and discussed in the context of further error sources.

1) Rainfall Rate: The uncertainty of the mean RR in a time bin is computed as the random error standard deviation of the mean RR in the time bin as follows:

$$\sigma_j^{\text{RR\_x}} = \frac{\sigma_{\Delta T, j}^{\text{RR\_x}}}{\sqrt{M}}, \quad j = 1, \dots, P \tag{10}$$

where j is the time-bin number ($P = 132$ bins in Fig. 1), $x = $ radar, disdrometer stands for the measurement instrument, $\sigma_{\Delta T, j}^{\text{RR\_x}}$ is the radar/disdrometer RR standard deviation for the jth bin computed from the 16-s samples ($\Delta T_{\text{master}} = 16$ s, Section II-B) in the bin, and M is the temporal-averaging ratio ($M = 5$, i.e., $80/16$).

2) Rain Extinction Coefficient: The random error standard deviation associated with the jth bin rain extinction coefficient [see (7)] is computed as follows:

$$\sigma_j^{\alpha\_\text{rain}} = \sqrt{\left(\sigma_j^\alpha\right)^2 + \left(\sigma_j^{\alpha\_\text{no\_rain}}\right)^2}, \quad j = 1, \dots, P \tag{11}$$

where σ_j^α is the error standard deviation of the total extinction coefficient for the jth bin (see (6) and Fig. 3(c), red circles) and $\sigma_j^{\alpha\_\text{no\_rain}}$ is the error standard deviation of the background extinction coefficient for the jth bin. In practice, because the background extinction is estimated shortly "before" and "after" the rain event (Fig. 3(b) and (c), purple and green traces, respectively), the background extinction for each bin in the rain interval is estimated by linear interpolation of the before- and after-rain extinction estimates.

Analogously, background extinction RMSE, $\text{RMSE}_j^{\alpha\_\text{no\_rain}}$, is computed in each bin by linear interpolation of the before- and after-rain RMSEs.

The error standard deviations σ_j^α and $\sigma_j^{\alpha\_\text{no\_rain}}$ in (11) above are associated with the respective extinction RMSEs

$$\sigma_j^\alpha = \text{RMSE}_j^\alpha, \quad \sigma_j^{\alpha\_\text{no\_rain}} = \text{RMSE}_j^{\alpha\_\text{no\_rain}}. \tag{12}$$

Equation (12) is justified because for an unbiased estimator, the mean squared error and the variance (equivalently, the RMSE and the standard deviation) of the estimator coincide. The slope method is an unbiased estimator for SNRs > 5 over the entire inversion range [44], and almost all of our cases shown here have SNR above this threshold.

Finally, it must be said that the slope method by itself is ambiguous because it leads to the conjecture $(1/\beta(h))|(d\beta(h)/dh)| \ll 2\alpha$ over small range intervals. There are situations, usually associated with cloud reflections or haze, where the combination of one inhomogeneous atmospheric extinction coefficient profile, $\alpha(h)$, with one inhomogeneous backscatter coefficient profile, $\beta(h)$, in differential lidar (4) above cannot be distinguished from a pair of homogeneous profiles, $\alpha(h) = \alpha$, $\beta(h) = \beta$ (see [52, Appendix A] for an analytical proof). In other words, although a homogeneous atmosphere is associated with virtually zero RMSE in the slope-method linear fit, the reverse is not always true. Therefore, usage of the RMSE as a quantitative indicator of atmospheric homogeneity must be interpreted with caution and is best evaluated with additional collocated instrumentation (Section IV-B).

IV. OBSERVATIONS

A. Outlook

Fig. 1 provides a quick overview of the rain episode: Fig. 1(a) shows the height-range profiles of the range-corrected attenuated backscatter signal measured by the ceilometer. Reddish colors are associated with high backscatter values caused by the presence of rain. Bluish colors are associated with very low backscatter levels, which delimit the ranges where the laser beam becomes extinguished due to the rain (usually, above 2 km) or where there is no rain [compare with Fig. 1(e) and (f)]. Below approximately 1.5 km, the falling rain traces draw diagonal streaks [53] in the height–time domain of Fig. 1(a). Thus, the rain curtain becomes shifted in time by 1–2 bins at ground level. The change in slope of these diagonal signatures over the entire analysis period [22:19–01:15 UTC, see also Fig. 1(b)] and, particularly, around 00:20–00:55 UTC suggests compression and dilation of the rain curtain, which can be indicative of the variations in the horizontal wind

component with time (i.e., horizontal shear varies with time) due to the episodic passage of the storm's outflow over the instrumented site. In Fig. 1(b), these diagonal signatures bend above approximately 2 km and follow a nearly vertical trace up to 3 km, which is indicative of light horizontal advection.

Fig. 1(b) shows the radar reflectivity factor computed from (2). In contrast to the ceilometer, the radar suffers from very little attenuation by rain, and hence, the rain curtain is clearly seen from 3 km (height of the bright band associated with the melting layer) downward. The rain event is stronger in the 22:30–00:30 UTC time interval and gets weaker afterward, ending at 01:15 UTC.

Fig. 1(c) shows the vertical velocity measured by the Doppler lidar. Bluish areas indicate negative velocities, hence corresponding to the fall velocities of raindrops. Greenish areas indicate near-zero velocities associated with the movement of aerosol particles which trace the vertical motion in the absence of rain. This behavior is corroborated in Fig. 1(d), which shows the Doppler lidar CNR. Thus, reddish and yellowish areas indicate high CNRs (i.e., strong returns, usually associated with rain), while greenish and bluish ones indicate low CNRs. Above approximately 2.2 km, the laser beams of both the ceilometer and the Doppler lidar become extinguished when the optical depth of the atmosphere is about 1.8. This is evidenced by bluish colors above this height in Fig. 1(a), noisy red-blue spikes in the vertical velocity profiles of the Doppler lidar [Fig. 1(c)], and bluish areas in Fig. 1(d), the latter indicative of low CNRs.

Fig. 1(e) plots the radar RR time series computed from (3) as a function of height, from 250 up to 2000 m (see legend). As expected from the falling delay of rain drops, the lower the radar measurement height, the longer the delay with respect to the 2000-m time series, which is the closest measurement height to the melting layer. Thus, the peak RR of 7 mm/h appearing at 22:02 UTC for the 2000-m RR time series, which corresponds to the onset of the rain episode, occurs at 22:03 for the 1500-m time series and, with lower intensity, at 22:06 for the 750 m one, and at 22:08 for 250 m one. This ordered set of RR series with height breaks up as we move on with time along the horizontal axis. The different amounts of horizontal shear with time, differential rain sedimentation, and size sorting may be contributing mechanisms, which cause the rain curtain [Fig. 1(a) and (b)] to slightly dilate and expand with time (a detailed study to disentangle these processes falls out of the scope of this work). In what follows, a reference height of 500 m has been chosen to compute the radar-retrieved products (reflectivity factor and RR). To justify this selection, we have opted for a best tradeoff between maximum correlation between the radar and the disdrometer RR time series [Fig. 1(e) and (f)] and being free from radar parallax effects.

Fig. 4(a) shows the cross-covariance function between the radar and the disdrometer RR time series. The cross-covariance (often called cross correlation or shifted dot product) measures the similarity between two time series by comparing one of them to a shifted (lagged) copy of the other. The maximum correlation coefficient as a function of height is obtained at 1-bin lag giving $\rho = 0.78$ (250 m),
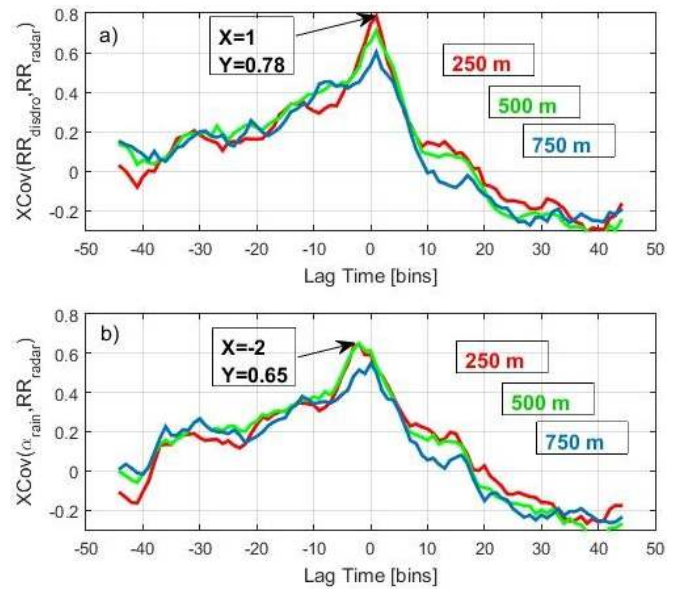

Fig. 4. Cross-covariance analysis (April 29–30, 2016) among the radar RR, the disdrometer RR, and the ceilometer extinction coefficient time series for different radar reference heights (250, 500, and 750 m). (a) Cross-covariance between the radar and the disdrometer RRs. (b) Cross-covariance between the radar RR and the ceilometer rain extinction.

$\rho = 0.71$ (500 m), and $\rho = 0.60$ (750 m). Although 250 m yields the highest correlation, at this height the parallax effect is still responsible for 1-dB attenuation in the radar reflectivity [33]. Above 750 m, the correlation coefficient starts to fall dramatically, which justifies selection of 500 m as the radar reference height. Similarly, when the radar RR is compared with the ceilometer extinction in Fig. 4(b), both 250 and 500 m in height attain similar maximum correlation, $\rho = 0.65$.

Using 500 m as the radar reference height [Fig. 1(e)], we continue our description of the rain episode shown in Fig. 1. The episode is roughly subdivided into three time intervals (vertical black lines) according to the three different rain regimes:

Time interval #1 (22:19–22:34 UTC) is the beginning of the rain episode and is characterized by a weak discontinuous rain curtain (2.7 mm/h on average measured by the disdrometer and 2.4 mm/h by the radar). The average rain extinction is $\alpha_{\text{rain}} = 0.15 \pm 0.06 km^{-1}$ (slope-method fitting interval, $I_1 = [0.3, 1.8]$ km, Fig. 3), and the average radar reflectivity factor at 500 m is 17.7 dBZ.

Time interval #2 (22:34–00:29 UTC) is the central portion of the rain event having the highest rain intensity (4.4 mm/h on average measured by the disdrometer and 4.6 mm/h by the radar). The average rain extinction coefficient is $\alpha_{\text{rain}} = 0.42 \pm 0.05$ km^{-1}, $I_2 = [0.8, 2.8]$ km) and the average radar reflectivity is 24.8 dBZ.

Time interval #3 (00:29–01:15 UTC) is the last interval of the rain event. Similar to interval #1, interval #3 is characterized by light intermittent rain. The precipitating cloud has advected over the site, and we are near the edge of it. The vertically pointing remote sensors are seeing fewer
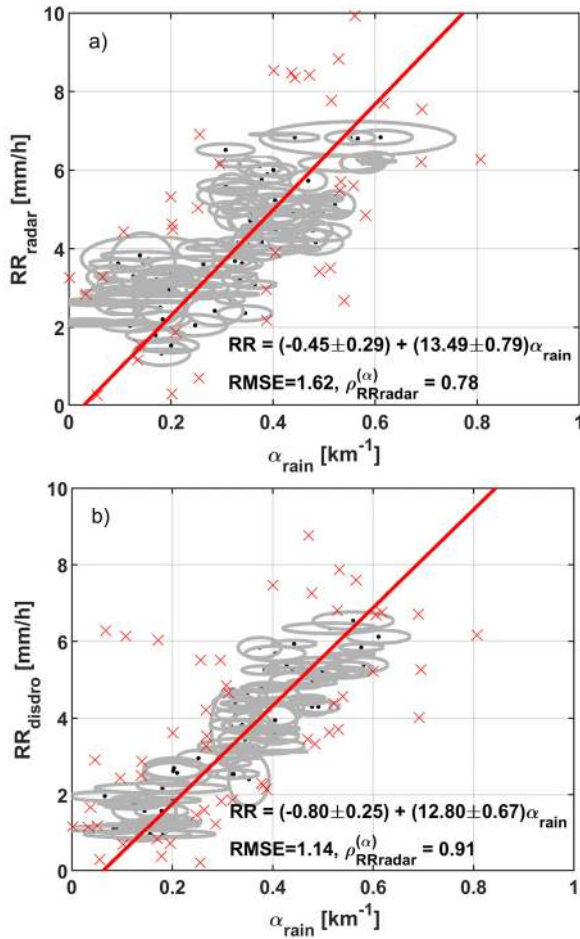
Fig. 5. RR–α model results (April 29–30, 2016). (a) Radar RR versus extinction estimates (radar reference height, $h = 500$ m). (b) Disdrometer RR versus extinction estimates. Red crosses indicate points rejected as outliers. (Red solid line) Linear fit with estimated errors. $\rho_{RR\_radar}^{(\alpha)}$ is the RR-to-rain-extinction correlation coefficient. Gray ellipses delimit the 1σ-uncertainty locus in each variable.

backscattering rain droplets in the downfall path because the rain is abating and the wind shear is moving the droplets away from them. This causes weak backscatter [Fig. 1(a)] and reflectivity [Fig. 1(b)] close to ground level and low disdrometer RRs [1.6 mm/h on average, Fig. 1(f)] when compared with the radar RRs at 500 m (2.8 mm/h, Fig. 1(e); average radar reflectivity, 19.4 dBZ). Similarly, the Doppler lidar shows near-zero vertical velocities (Fig. 1(c), greenish patches) and low CNRs (-30 dB, bluish shades) close to ground level. The average rain extinction is $\alpha_{rain} = 0.19 \pm 0.07$ km^{-1} ($I_3 = [0.5, 2.4]$km), similar to that of interval #1.

B. RR-to-Extinction Intercomparison

Fig. 5 shows the comparison results for the ceilometer–radar and ceilometer–disdrometer pairs according to the RR–α model (Section I)

$$RR = a + b\alpha_{rain} \qquad (13)$$

with a and b representing the fitting parameters. The linear model is proposed on account of the small range of RR–α

values, which is the case of the ceilometer that is not capable of providing estimates in high RRs. To estimate the fitting parameters in (13), the outlier rejection criteria were first applied and then the fitting parameters above were solved using York's fitting method [54], which assimilates errors in both the x- and y-variables (α_{rain} and RR, respectively). RMSE is computed as the York-weighted RMSE. These two steps are discussed next:

Outlier Rejection Criteria: Two main types of outliers have been identified in Fig. 5(a): Type-1 outliers are due to time variation in the rainfall character. Examples include the effect of horizontal wind shear, which causes sudden time/space changes in the slope of the diagonal signature of the rain curtain [e.g., 00:27–00:42 UTC, Fig. 1(a) and (d)] and temporal inhomogeneities in the rain intensity (e.g., intermittent rain, 00:42–00:54 UTC). As a consequence of the latter, rain advected from adjacent time bins into the current bin being analyzed results in similar column extinction values measured by the ceilometer at different time bins being associated with very different RRs. In Fig. 5(a), this gives rise to a large span of extinction values associated with a particular RR bin (e.g., 2–3- and 6–7-mm/h RRs).

Type-2 outliers account for those cases in which the slope method to retrieve the extinction coefficient in the current time bin results in a fit that is comparatively poorer than for other time bins (i.e., yields a much higher RMSE) due to the failure of the atmospheric homogeneity hypothesis in the height-fitting interval (Section III-B). This is a limitation of the semiautomated fitting procedure, which uses the same starting/end fitting ranges over predefined time subintervals (chosen manually) instead of individualized ones for each time bin.

Fig. 6(a) shows the histogram of the radar RRs plotted in Fig. 5(a) (i.e., the ordinates of the points therein; the statistical sample consists of 132 points) and Fig. 6(b) shows the histogram of the rain extinction coefficients for one example bin (the 4–5-mm/h bin) of the RR histogram in Fig. 6(a). Thus, the 4–5-mm/h histogram of Fig. 6(b) plots the rain extinction associated with 4–5-mm/h points in Fig. 5(a). The shape of the distribution of the rain extinction in the different RR bins is similar to the one shown in Fig. 6(b) with slight bimodality for the 2–3-mm/h bin (not shown). Table III shows the 16th and 84th percentiles (PCs) of the extinction for each RR bin.

To reject outliers, we limit the spread of both the RR and the extinction distributions by excluding points that fall out of the acceptance interval

$$[\mu_{RR/\alpha} - n_{RR/\alpha} \cdot \sigma_{RR/\alpha}, \mu_{RR/\alpha} + n_{RR/\alpha} \cdot \sigma_{RR/\alpha}] \quad (14)$$

where μ is the mean of the distribution, σ is the standard deviation, n is the standard deviation factor defined as the number of standard deviations away from the mean, and subscripts RR and α refer to the "rainfall rate" and "extinction," respectively. Equation (14) is applied first to the overall RR distribution [type-1 outliers, Fig. 6(a)] and second to the rain extinction distribution associated with each successive 1-mm/h bin of the RR distribution [type-2 outliers, Fig. 6(b)].

The RR histogram [Fig. 6(a)] shows a slightly skewed distribution, which is often the case for precipitation
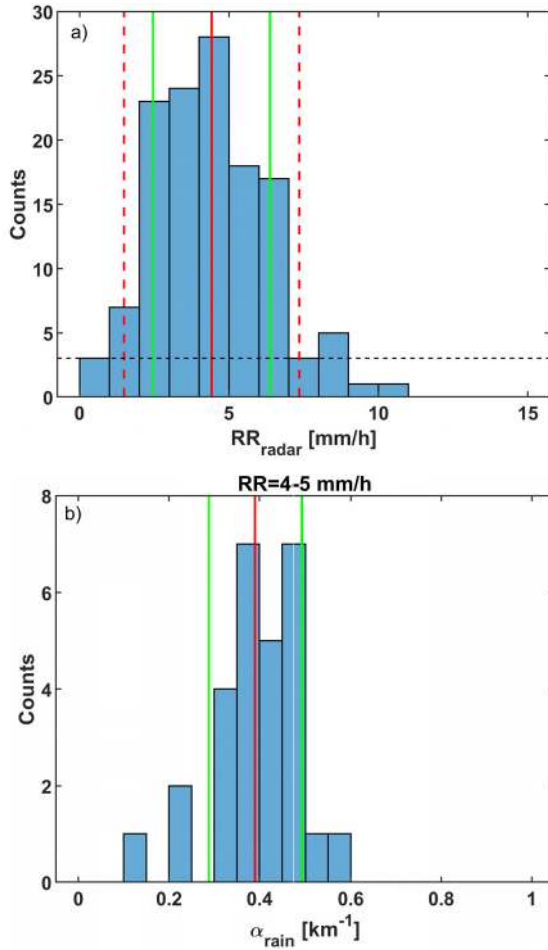
TABLE III

COMPARISON BETWEEN 16TH AND 84TH PCS OF THE GAUSSIAN
DISTRIBUTION AND THOSE OF THE MEASURED RAIN EXTINCTION
DISTRIBUTION FOR EACH RR BIN (RADAR CASE)

RR bin [mm/h]	No. of extinction bins	μ [km^{-1}]	Gaussian $\mu - 1\sigma$ [km^{-1}]	$\mu + 1\sigma$ [km^{-1}]	Measured 16-th pc [km^{-1}]	84-th pc [km^{-1}]
0-1	3	0.17	0.07	0.27	0.06	0.26
1-2	7	0.17	0.15	0.20	0.14	0.20
2-3	23	0.20	0.06	0.33	0.05	0.34
3-4	24	0.24	0.11	0.37	0.11	0.36
4-5	28	0.39	0.29	0.49	0.32	0.48
5-6	18	0.40	0.30	0.51	0.31	0.53
6-7	17	0.49	0.34	0.65	0.31	0.61
7-8	3	0.61	0.52	0.70	0.51	0.69
8-9	5	0.46	0.41	0.50	0.41	0.51
9-10	1	0.56	0.56	0.56	0.56	0.56
10-11	1	0.69	0.69	0.69	0.69	0.69

μ: mean. σ: standard deviation. 16-th and 84-th Gaussian percentiles are computed as $\mu - 1\sigma$ and $\mu + 1\sigma$, respectively. μ and $\mu \pm 1\sigma$ values shown for the 4-5-mm/h bin correspond to the vertical lines plotted in Fig. 6b.

Fig. 6. Radar-RR and extinction histograms (April 29–30, 2016). (a) Radar-RR histogram. Bin-width is 1 mm/h. Red solid line indicates the mean RR (μ_{RR}), green solid lines delimit the acceptance interval at 1σ (i.e., $n_{RR} = 1$), and red dashed lines at 1.5σ. Black horizontal dashed line is set at three counts. (b) Histogram of the rain extinction coefficient for the 4–5-mm/h RR bins in (a). Bin-width is 0.05 km^{-1}. Red solid line indicates the mean value (μ_α), and the green solid lines delimit the acceptance interval at 1σ (i.e., $n_\alpha = 1$).

(log-normal, [55]), but which is not far from the shape of a Gaussian. We hypothesize that this Gaussian-like distribution is a consequence of the fact that the distribution merges into a single body not only the precipitation distribution itself but also that of the many different additive error sources at play. The sum distribution, on account of the central limit theorem, approaches the Gaussian when the number of sources tends to infinity [56]. For an approximately normal data set, the values within one standard deviation of the mean ($\mu \pm 1\sigma$) account for about 68% of the set or, equivalently, to the population between 16th (exactly, 15.9) and 84th (84.1) PCs ($\mu - 1\sigma$ and $\mu + 1\sigma$, respectively). Table III corroborates the goodness of the Gaussian approximation within the approximate $\pm 1\sigma$ limits of the accepted extinction samples by showing virtually coincident PCs between the normal and the measured distribution. For highly skewed distributions, the "split histogram" method [57] is a good alternative.

When rejecting type-1 outliers, standard deviation factors between $n_{RR} = 1 - 1.5$ [see (14)] yielded similar model-fitting results (Fig. 5) while keeping the central bins of the distribution. With the choice, $n_{RR} = 1.5$, 19 samples were rejected (14% of the population), keeping as valid data the large amount of samples between 2–3 and 6–7 mm/h. Concerning type-2 outliers, extinction histograms computed for each 1-mm/h bin [Fig. 6(b)] contained a much smaller number of samples, such that the shape of the distribution was not well-reproduced. By choosing the factor $n_\alpha = 1$, most of the tallest bins were accepted (approximately, full width half height of the distribution), while for $n_\alpha \geq 2$ all the bins were accepted, therefore providing no filtering at all. After manual inspection of a set of 20 rejected samples (15% of the population), only two samples were found to be wrongly rejected ($<10\%$).

1) York's Fitting: York's method [54] is a covariance-weighted method of fitting used to compute the best straight line fit to data points having normally distributed errors on both the x- and y-components. The algorithm assigns weights to both the x- and y-variables (bivariate method) and uses a recursive procedure to estimate the fit slope, intercept, and their associated uncertainties under a maximum likelihood estimation criterion. A further output of the algorithm is the so-called "weighted RMSE" of deviations from the best-fit line computed, which can be considered a "goodness-of-fit" parameter [58].

The input errors to York's method (rain extinction and RR errors) have been computed according to (10)–(12) above. The estimated model parameters [see (13)], $a = -0.45 \pm 0.29$, $b = 13.49 \pm 0.79$ [ceilometer–radar; Fig. 5(a)], and $a = -0.80 \pm 0.25$, $b = 12.80 \pm 0.67$ [ceilometer–disdrometer; Fig. 5(b)] show comparatively lower uncertainties for the RR–α ceilometer–disdrometer model. Similarly, the weighted RMSEs for the radar and disdrometer fits are 1.6 and 1.1 mm/h, respectively. This behavior can be explained by the fact that the temporal variability of the RR due to the effects of the horizontal and vertical wind components is higher at the radar reference height (500 m) than at ground level. Fig. 5 also
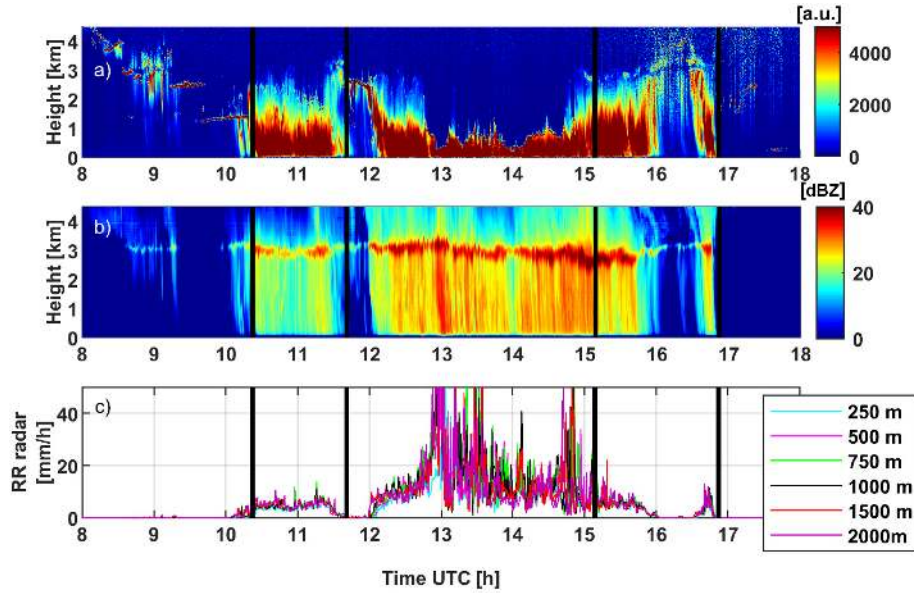
Fig. 7. Overview of March 31, 2016, rain episode. (a) Ceilometer range-corrected lidar signal [a.u.] versus time. (b) Radar reflectivity factor [dBZ] computed after (22). (c) RR [mm/h] time series measured by the radar at different heights, from 250 up to 2000 m. Vertical lines delimit the early-and late-morning time intervals discussed in Section V. Temporal resolution [(a)–(c)] is 16 s. Spatial (height) resolution [(a)–(c)] (see Table I).

shows slightly lower RRs for the disdrometer than for the radar. Thus, for rain extinctions between 0.3 and 0.4 km^{-1}, the mean radar RR is 4.8 mm/h [Fig. 5(a)], while the mean disdrometer RR is 3.7 mm/h, about a 23% lower. A plausible explanation lies on the very different measurement sensitivities of the radar (which is sensitive to the sixth moment of the size distribution) and the disdrometer (which is sensitive to the volume of the rain, third moment of the size distribution). Overall, the RR–α correlation coefficients for the 132-bin data set of Fig. 5 are $\rho^{(\alpha)}_{\text{RR\_radar}} = 0.78$ (0.68 without outlier rejection) and $\rho^{(\alpha)}_{\text{RR\_disdro}} = 0.91$ (0.71 without).

2) Error Due to the Uncertainty in the Aerosol Extinction Coefficient ($\alpha_{\text{no\_rain}}$): Following our discussion after (7), depending on the RR, we easily have a 50% reduction in the aerosol extinction just after the rain episode [$\alpha^{\text{no\_rain}}_{\text{before}} = 0.09 \pm 0.02$ km^{-1}, $\alpha^{\text{no\_rain}}_{\text{after}} = 0.02 \pm 0.05$ km^{-1}, Fig. 3(c)]. The resulting impact on the derived RR of, for example, a $0.05 - $ km^{-1} overestimation error in the aerosol extinction ($\Delta\alpha_{\text{no\_rain}} = \hat{\alpha}^{\text{no\_rain}}_{\text{after}} - \alpha^{\text{no\_rain}}_{\text{after}} = 0.05$ km^{-1}, the "hat" means the estimated value) is a systematic error $\Delta\text{RR} = -b \cdot \Delta\alpha_{\text{no\_rain}} \approx -0.7$mm/h [see (7) and (13)], which is particularly significant for small RRs. Graphically, this bias is equivalent to shifting the fit line of Fig. 5(a) and (b) slightly to the right.

V. ADDITIONAL CASE STUDY: MODEL VERIFICATION

The methodology presented in Sections II-B, III, and IV has been applied to a different rain event, March 31, 2016 (Fig. 7). During this event, the disdrometer was not deployed at Belle Mina, so only the radar RR–α model will be evaluated for this event. The event is subdivided into two time intervals, one in the early morning (10:22–11:41 UTC, in what follows the "early-morning period") and one in the late morning (15:09–16:52 UTC, "late-morning period"; local time,

LT = UTC-5). The time interval between these two periods above (12:51–14:48 UTC) is not considered because the rain intensity is comparatively so high (16.2 mm/h, 27.6 dBZ) such that the ceilometer signal becomes fully extinguished in a very short distance (300–800 m), which does not allow successful application of the slope method (see Section III-B).

In comparison to Fig. 1, the rain curtain is fairly uniform over the 0–3-km layer, indicating either that the horizontal winds may be weaker than in the April 29–30, 2016, case or that the source region for the precipitation is more uniform over a larger area. The radar RRs in the two selected periods are also more uniform over a wider range of heights than in the April 29–30, 2016, case [Fig. 7(c)]. In the selected early- and late-morning periods, the mean RR (radar reflectivity factor) is 4.4 (20.2 dBZ) and 4.1 mm/h (19.6 dBZ), respectively, similar to the values found in the previous case (April 29–30, 2016; Section IV-A, Fig. 1). Following analogous cross-covariance analysis [Fig. 4(b)], the chosen radar reference height is 500 m.

Fig. 8 shows the profile of the rain extinction coefficient during the early- and late-morning periods. The average extinction coefficient during the early-morning event is $\alpha_{\text{rain}} = 0.34 \pm 0.05$ km^{-1} ($I_1 = [0.5, 2.5]$ km) and $\alpha_{\text{rain}} = 0.29 \pm 0.06$ km^{-1} ($I_2 = [0.3, 2.5]$ km) during the late-morning event (I_1 and I_2 indicate the slope-method fitting range intervals used). The estimated background extinction coefficients before and after the rain episode are as follows: $\alpha^{\text{no\_rain}}_{\text{before}} = 0.11 \pm 0.02$ km^{-1} (08:24–08:26 UTC; $I_{\text{before}} = [0.3, 1.0]$ km) and $\alpha^{\text{no\_rain}}_{\text{after}} = 0.02 \pm 0.06$ km^{-1} (17:10–17:34 UTC; $I_{\text{after}} = [0.3, 1.3]$ km). These background extinction figures are similar to the ones obtained for the April 29–30 event (Section IV-A) and again substantially lower than the average rain extinction coefficients above, which suggests that the aerosol is being removed (scavenged) by the precipitation.
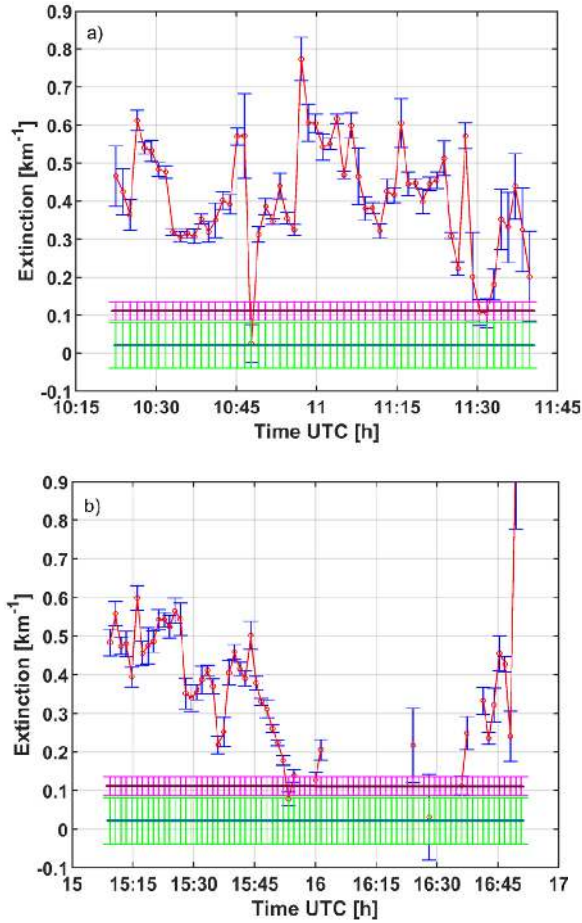
Fig. 8. Slope-method results (Belle Mina, March 31, 2016). Time resolution 80 s and spatial resolution 200 m. (a) Early-morning rain interval, 10:22–11:41 UTC. 59 time bins. Same as Fig. 3(c). (b) Late-morning rain interval, 15:09–16:52 UTC. 46 bins.

A. RR-to-Extinction Model

The methodology of Section IV-B has been used to estimate (13) RR–α model. Three different sets of data have been considered when deriving the fit parameters: the early-morning period, the late-morning period, and a third data set composed by joining the early-morning and late-morning data sets. York's linear-fitting results are shown in Fig. 9. The uncertainties of the fit for the early-morning period [Fig. 9(a)] are indeed larger than for the late-morning period [Fig. 9(b)] as shown by higher uncertainties in the estimated slope and intercept point, and higher RMSE (York's weighted RMSE = 1.49). The modest correlation coefficient obtained during the early-morning period ($\rho_{RRradar}^{(\alpha)}$ = 0.54, which would be 0.51 without excluding outliers) is a consequence of the relatively narrow span of RR figures experienced during this period [roughly 3–6 mm/h, 10:22–11:41 UTC, Fig. 7(c)]. The situation in the late morning is different because the late-morning period includes the final part of the rain event (15:09–16:52 UTC) when there was a marked decay in the rain intensity. As a result, a wider span of RR estimates is available although with fewer measurements (46 samples in the late-morning case when compared with 59 in the early-morning case). Relative to the early-morning figures,
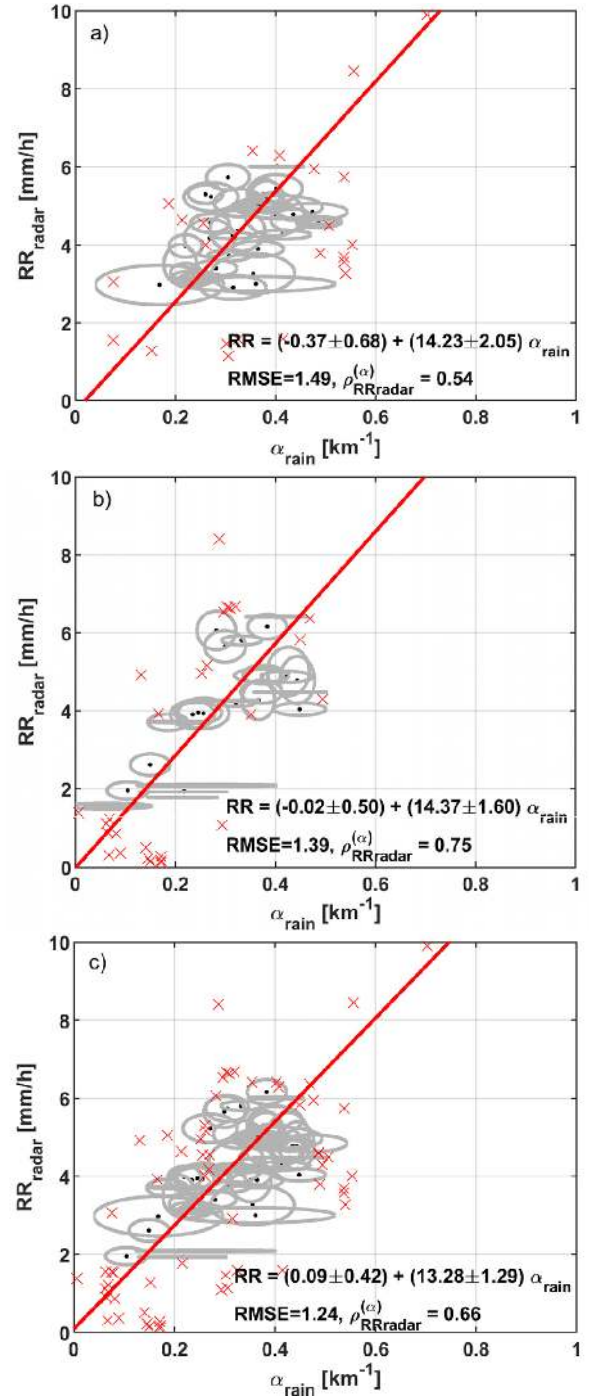

Fig. 9. RR–α model results (Belle Mina, March 31, 2016). (a) Radar RR versus extinction estimates (radar reference height, $h = 500$ m), early-morning period. (b) Late-morning period. (c) Early- and late-morning periods combined together. Same format as Fig. 5.

the late-morning RMSE decreases to 1.39 and the correlation coefficient increases to $\rho_{RRradar}^{(\alpha)} = 0.75$.

Even though the uncertainties are larger in the early-morning period, the data are still useful. When both early- and late-morning periods are merged as a whole [Fig. 9(c)], the RR–α model benefits from a larger statistical sample (102) and a wider span of RRs. We derive similar RR–α model parameters but with much lower uncertainties. The combined
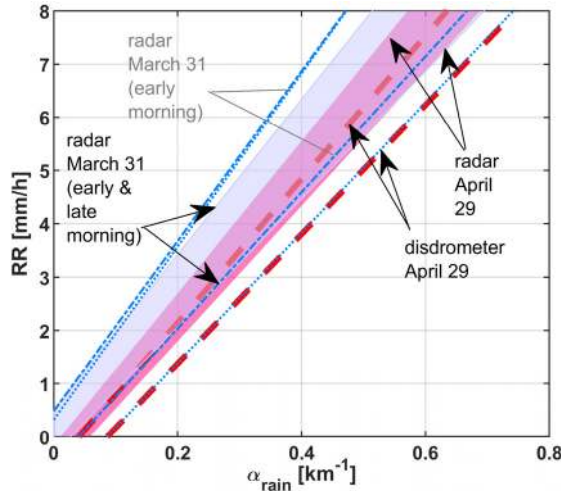
Fig. 10. Comparison between April 29 and March 31 RR–α models (see text).
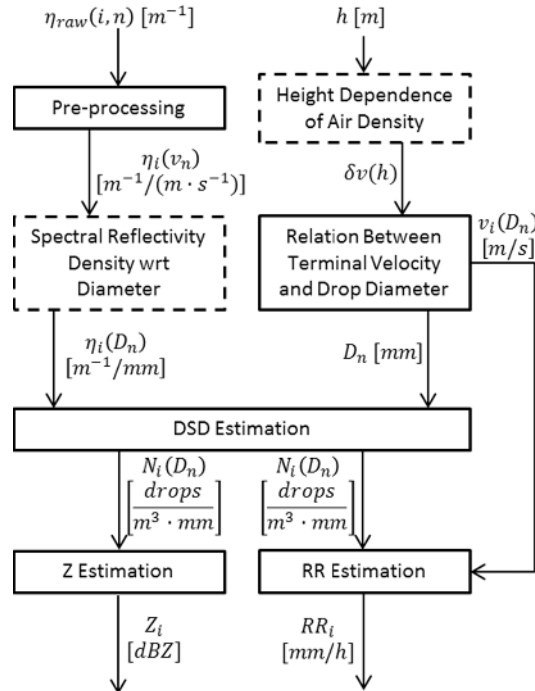

Fig. 11. Algorithm block diagram used to estimate the RR and radar reflectivity factor from S-band FMCW radar measurements.

RMSE also decreases to 1.24 mm/h, which is indicative of a higher goodness of fit.

Finally, Fig. 10 intercompares the RR–α models obtained for the cases April 29 (Section IV) and March 31 (Section V). April 29 case is described by the purple patch and dashed red lines. Purple patch represents the uncertainty locus associated with the radar-RR-to-α model of Fig. 5(a) (i.e., due to uncertainties in the linear fit parameters, see equation in Fig. 5(a) legend). Dashed red lines delimit the uncertainty locus associated with the disdrometer-RR-to-α model of Fig. 5(b). For the March 31 case, the gray patch represents the uncertainty locus associated with the radar-RR-to-α model of Fig. 9(c) (early + late morning). The early-morning case [Fig. 9(a)]

is delimited by thin blue dotted lines and the late-morning case [Fig. 9(b)] by blue dash-dotted lines (not shown, lines are virtually coincident and cannot be individually spotted). For the radar–ceilometer pair, the uncertainty locus of April 29 model virtually overlaps that of March 31, which evidences that the method is consistent across these two cases.

In addition, the April 29 uncertainty region falls inside that of March 31, showing that model uncertainties are lower for the April 29 case (which benefits from a larger number of samples). When the disdrometer–ceilometer pair is considered (available for April 29 case only), the disdrometer RR–α model (dashed red lines) also overlaps the radar RR–α model (both days), although its RRs are biased slightly lower (by approximately -0.5 to -1.5 mm/h). It is evident that some combination of systematic errors is preventing a closer match between RRs, possibly including the different sensitivities on what the different techniques measure, size sorting due to differential rain sedimentation, and the variations in horizontal wind speed and direction during the passage of the storm.

VI. CONCLUSION

RRs under low-to-moderate rain conditions have successfully been retrieved from vertically pointed, 905-nm wavelength, ceilometer measurements of the optical extinction coefficient using relationships developed through comparison with the S-band radar and the disdrometer. Because the sensitivity of commercial lidar ceilometers is limited, the method's applicability is restricted to RRs below approximately 10 mm/h. Two different test days from VORTEX (March 31 and April 29–30, 2016) have been considered. The weighted RMSEs (York's weighted square root of the variance of the residuals) after fitting a linear RR–α model [see (13)] to the ceilometer extinction and RR data are 1.6 (radar RR) and 0.9 mm/h (disdrometer RR) for the April 29 case and 1.2 mm/h (radar RR) for the March 31 case. A summary plot of the model uncertainty locus versus RR is shown in Fig. 10. A wide span of the measured RR values is beneficial for regression analysis.

The rain extinction coefficient has been retrieved using a differential formulation of the slope method [28] in which the height-averaged extinction is computed by subtracting the "no-rain" background extinction from the measured extinction under rainy conditions. The time series of the extinction coefficient (Figs. 3(c) and 8) has been estimated by successive application of the method over adjacent time bins of width smoothed temporal resolution (80 s). The radar-retrieval procedure is summarized in Fig. 11.

When comparing the ceilometer-retrieved extinction set with the radar/disdrometer RRs, the different instruments and temporal and spatial resolutions involved pose an intercomparison difficulty (Section III). Thus, while the ceilometer provides height-resolved attenuated backscatter information, the slope-method retrieved extinction is a height-averaged product under the assumption of atmospheric homogeneity. Although there are many different error sources affecting both the measured ceilometer rain extinction and the radar/disdrometer measured RRs, an attempt to quantify the most important ones has been made.

A first potential error source was the uncertainty in the estimated rain extinction coefficient. This error source was estimated by error-propagating the uncertainties in the slope used to derive the total extinction under rain conditions and the background extinction from the ceilometer attenuated backscatter measurements. The second error source was the assumption that the aerosol extinction is unaffected by the precipitation. This error source was addressed by estimating the background extinction in closely spaced measurements before and after the rain event. York's method was used to estimate significant uncertainties associated with the linear regression coefficients in the empirical RR–α model used to derive the RR from extinction measurements. The uncertainty in the background aerosol extinction had the largest impact when the RR was small (e.g., an overestimation of 0.05 km^{-1} translated into systematic error of -0.7 mm/h). For higher RRs, the impact of this error source was small to negligible. At higher RR values, RR estimation from ceilometer measurements was essentially limited by optical thicknesses around 1.8, which dramatically reduced the maximum measurement height to a few hundred of meters and impeded application of the slope method.

Third, and central to the slope method, is the assumption of a homogeneous atmosphere, or equivalently, a homogeneous rain curtain, which may be hampered by many different mechanisms (e.g., sudden changes in the wind horizontal speed (shear) and direction advecting the raindrops at different levels, rain streaks moving in and out of the probing column, microphysical processes). Such mechanisms can be responsible for irregular signatures and contraction and dilation of the rain curtain, which contributed to decouple the column extinction measured by the ceilometer with respect to the RR measured by the radar at the given reference height (500 m), and which translated into a bias when comparing the disdrometer RR with the radar RR.

Finally, the fact that a manual process (guided under a minimum RMSE criterion) was used to select the height interval over which the slope method was derived might be yielding slightly higher extinction error bars over time intervals with larger inhomogeneities (beginning and end or the rain episode) or close to the melting layer.

APPENDIX

The steps to estimate the radar reflectivity factor (Z) and RR as a function of height from the radar volume reflectivity follow those described in [10] and [59] and are shown in Fig. 11.

The first block in the upper left branch of Fig. 11 is the preprocessing block. This block is aimed at removing artifacts such as insects or the effect of ground clutter. The input of this block is the raw volume spectral reflectivity, $\eta_{\text{raw}}(i, n)$, as a function of range and velocity index. This block computes the clean volume spectral reflectivity density, hereafter the reflectivity density, as $\eta_i(f_n) = \eta_{\text{raw}}(n, i)/\Delta f [\text{m}^{-1}/\text{Hz}]$. At the output of the preprocessing block, the reflectivity density with respect to the velocity, $\eta_i(v_n)[\text{m}^{-1}/(\text{m} \cdot \text{s}^{-1})]$, is computed as follows using that $d\eta = \eta(v_n)dv_n = \eta(f_n)df_n$:

$$\eta_i(v_n) = \eta_i(f_n)\frac{\partial f_n}{\partial v_n} \tag{15}$$

where $\partial f_n/\partial v_n = 2/\lambda$ from the basic Doppler relationship of (1). It is important to note that whereas the input the preprocessing block is a reflectivity, its output is a reflectivity density.

The DSD, $N(D)$ [drops/(m$^3 \cdot$mm)], has been modeled using theoretical size distributions by several authors including [4] and [60]–[63]. The DSD is defined as the ratio of the reflectivity density with respect to the drop diameter, $\eta(D)$ [m^{-1}/mm], to the single-particle backscattering cross section of a drop of diameter D, $\sigma(D)$ [m^2/drop]. That is, the number of drops per unit volume and diameter

$$N(D) = \frac{\eta(D)}{\sigma(D)}. \tag{16}$$

For spherical raindrops, which is a reasonable assumption for small drops, and because the size of a raindrop is much smaller than the radar wavelength (i.e., $D \leq \lambda/16$, Rayleigh approximation), the backscattering cross section is well-approximated by that of a spherical raindrop, $\sigma(D) = (\pi^5/\lambda^4)|K_w|^2 D^6$, where $K_w = (m^2-1)/(m^2+2)$ and m is the complex refractive index of water. For nonspherical raindrops, the diameter is defined as the drop-volume equivalent diameter. $|K_w|^2 \approx 0.92$ for water at the radar operating frequency (2.94 GHz) and it is practically independent of temperature [10], [64]. This analytical expression of the backscattering cross section enables us to rewrite (16) as follows:

$$N(D_n) = \frac{\eta(D_n)}{D_n^6}\frac{\lambda^4}{\pi^5}\frac{1}{|K_w|^2} \tag{17}$$

where D_n stands for the discrete set of diameters. In (17), diameter D has been changed to discrete variable D_n to relate D_n to the Doppler velocity set v_n. In addition, the range index i has been omitted in the reflectivity density $\eta(D_n)$ because the Doppler spectra are computed at a given range (or reference height).

To compute the DSD (see (17) above), two steps are needed: 1) to relate the reflectivity density as a function of drop diameter to the reflectivity density as a function of velocity [see (15)] and 2) to compute the discrete raindrop diameter set, D_n, from the Doppler velocity set, v_n, [see (1)].

To complete the first step, we rearrange $d\eta = \eta(D_n)dD_n = \eta(v_n)dv_n$ to yield

$$\eta(D_n) = \eta(v_n)\frac{\partial v_n}{\partial D_n} \tag{18}$$

where $(\partial v_n/\partial D_n)$ addresses the relationship between the terminal fall velocity and the drop diameter [65]. The analytical form of the velocity–diameter model was given in [66] and is computed for $0.109 \leq D \leq 6$ mm by the top-right branch blocks of Fig. 11 as follows:

$$v(D_n) = (9.65 - 10.3e^{-0.6 \cdot D_n})\delta v(h) \tag{19}$$

where $v(D_n)$ is the terminal velocity as a function of drop diameter and $\delta v(h)$ is the height-dependent density correction for the terminal fall velocity [67]

$$\delta v(h) = 1 + 3.68 \cdot 10^{-5}h + 1.71 \cdot 10^{-9}h^2 \tag{20}$$

and where h is the height in meters, $h = i\Delta h$, with Δh the height resolution. The model used in (20) assumes U.S.

standard atmosphere conditions and is based on the terminal-velocity-to-air-density relationship, $v \propto \rho^{0.4}$.

Taking the derivative with respect to D_n of (19) yields

$$\frac{\partial v_n}{\partial D_n} = 6.18 e^{-0.6 D_n} \delta v(h). \tag{21}$$

Combining the reflectivity density with respect to the velocity, $\eta_i(v_n)$, which is available at the output of the preprocessing block, with the derivative of velocity with respect to the diameter computed by (21), we obtain the sought-after $\eta(D_n)$ [see 18] to be inserted in (17). This completes the first step to compute the DSD.

For the second step, we solve (19) for D_n, that is, $D_n = -(1/0.6)\ln[(9.65/10.3) - (v_n/10.3\delta v(h))]$, to compute the raindrop diameter set, D_n, given the discrete and uniformly spaced Doppler velocity set, v_n [see (1)]. Because of the log-transformation involved, the diameter set, D_n, becomes nonuniformly spaced with diameter resolution, $\Delta D_n = (\partial D_n/\partial v_n)|_{v_n} \Delta v$. We thereby obtain an equation for $N(D_n)$ in terms of velocity v_n only. From these two steps, the DSD [see (17)] can readily be computed for each range gate (see block "DSD Estimation" in Fig. 11). The last two blocks of Fig. 11 concern the estimation of the RR and the radar reflectivity factor, Z. The RR [mm/h], which is defined by (3) in the main text, is computed by replacing integration by summation over the discrete size range and dD by ΔD_n. The input variables for the RR estimation block are the DSD and the terminal velocity as a function of discrete diameter, D_n.

The DSD is used to both estimate the RR and the radar reflectivity factor independently of the measured RR (e.g., Z–RR relationships [64], [68]). The reflectivity factor is defined as the sixth power of the raindrop diameter summed over all the size distribution [see (2)], and it is numerically computed in similar fashion as the RR (see (3) by the "Z estimation" block of Fig. 11).

As final remark, the reflectivity factor from (2) can alternatively be computed as the well-known equivalent reflectivity factor, Z_e, which is related to the volume reflectivity $\eta[m^{-1}]$ as $Z_e = (\lambda^4/\pi^5)(1/|K_w|^2)\eta$ [10]. This reflectivity factor is rewritten next as a function of the reflectivity density with respect to the diameter, $\eta = \int_0^\infty \eta(D)dD$, as follows:

$$Z_e = \frac{\lambda^4}{\pi^5} \frac{1}{|K_w|^2} \int_0^\infty \eta(D)dD. \tag{22}$$

Note that combining (2) and (22) over an integration (summation) bin, $dD = \Delta D_n$, results in (17).

ACKNOWLEDGMENT

REFERENCES

[1] VORTEX-SE. *VORTEX-SE*. The National Severe Storms Laboratory (NSSL). Accessed: Nov. 23, 2017. [Online]. Available: http://www.nssl.noaa.gov/projects/vortexse/

[2] R. Tanamachi, S. J. Frasier, W. Heberling, J. Waldinger, M. Seedorf, and J. Bozell, "Purdue-UMass mobile radar observations collected during VORTEX-Southeast 2016," in *Proc. Results VORTEX-SE Field Program, Session 28th Conf. Severe Local Storms*, 2016, Paper 3.6. [Online]. Available: https://ams.confex.com/ams/28SLS/webprogram/Paper301419.html

[3] T. J. Wagner, P. M. Klein, and D. D. Turner, "A new generation of ground-based mobile platforms for active and passive profiling of the boundary layer," *Bull. Amer. Meteorolog. Soc.*, vol. 100, no. 1, pp. 137–153, Jan. 2019.

[4] J. S. Marshall and W. M. Palmer, "The distribution of raindrops with size," *J. Meteorol.*, vol. 5, pp. 165–166, Aug. 1948.

[5] J. W. Telford, "A new aspect of coalescence theory," *J. Meteorol.*, vol. 12, no. 5, pp. 436–444, Oct. 1955.

[6] M. Komabayasi, T. Gonda, and K. Isono, "Life time of water drops before breaking and size distribution of fragment droplets," *J. Meteorolog. Soc. Jpn. Ser. II*, vol. 42, no. 5, pp. 330–340, 1964.

[7] C. W. Ulbrich and D. Atlas, "Assessment of the contribution of differential polarization to improved rainfall measurements," *Radio Sci.*, vol. 19, no. 1, pp. 49–57, Jan. 1984.

[8] C. R. Williams and K. S. Gage, "Raindrop size distribution variability estimated using ensemble statistics," *Annales Geophysicae*, vol. 27, no. 2, pp. 555–567, 2009.

[9] H. R. Pruppacher and R. L. Pitter, "A semi-empirical determination of the shape of cloud and rain drops," *J. Atmos. Sci.*, vol. 28, no. 1, pp. 86–94, Jan. 1971.

[10] J. R. Doviak and D. S. Zrnić, *Doppler Radar and Weather Observations*, 2nd ed. New York, NY, USA: Dover, 2006.

[11] C. D. Westbrook, R. J. Hogan, E. J. O'Connor, and A. J. Illingworth, "Estimating drizzle drop size and precipitation rate using two-colour lidar measurements," *Atmos. Meas. Techn.*, vol. 3, no. 3, pp. 671–681, 2010.

[12] R. R. Rogers, "A review of multiparameter radar observations of precipitation," *Radio Sci.*, vol. 19, no. 1, pp. 23–36, Jan. 1984.

[13] W. F. Krajewski and J. A. Smith, "Radar hydrology: Rainfall estimation," *Adv. Water Resour.*, vol. 25, nos. 8–12, pp. 1387–1394, Aug. 2002.

[14] E. I. Nikolopoulos, A. Kruger, W. F. Krajewski, C. R. Williams, and K. S. Gage, "Comparative rainfall data analysis from two vertically pointing radars, an optical disdrometer, and a rain gauge," *Nonlinear Processes Geophys.*, vol. 15, no. 6, pp. 987–997, 2008.

[15] V. Chandrasekar, S. Lim, and E. Gorgucci, "Simulation of X-band rainfall observations from S-band radar data," *J. Atmos. Ocean. Technol.*, vol. 23, no. 9, pp. 1195–1205, Sep. 2006.

[16] G. Kathiravelu, T. Lucke, and P. Nichols, "Rain drop measurement techniques: A review," *Water*, vol. 8, no. 1, p. 29, 2016.

[17] W. F. Krajewski *et al.*, "DEVEX-disdrometer evaluation experiment: Basic results and implications for hydrologic studies," *Adv. Water Resour.*, vol. 29, no. 2, pp. 311–325, Feb. 2006.

[18] U. Saeed, F. Rocadenbosch, and S. Crewell, "Adaptive estimation of the stable boundary layer height using combined lidar and microwave radiometer observations," *IEEE Trans. Geosci. Remote Sens.*, vol. 54, no. 12, pp. 6895–6906, Dec. 2016.

[19] S. Kotthaus *et al.*, "Recommendations for processing atmospheric attenuated backscatter profiles from vaisala CL31 ceilometers," *Atmos. Meas. Techn.*, vol. 9, no. 8, pp. 3769–3791, 2016.

[20] H. C. van de Hulst, *Light Scattering by Small Particles*. New York, NY, USA: Wiley, 1957.

[21] D. B. Rensch and R. K. Long, "Comparative studies of extinction and backscattering by aerosols, fog, and rain at 106 μ and 063 μ," *Appl. Opt.*, vol. 9, no. 7, p. 1563, Jul. 1970.

[22] H. R. Pruppacher and K. V. Beard, "A wind tunnel investigation of the internal circulation and shape of water drops falling at terminal velocity in air," *Quart. J. Roy. Meteorolog. Soc.*, vol. 97, no. 411, pp. 133–134, Jan. 1971.

[23] H. Vasseur and C. J. Gibbins, "Prediction of apparent extinction for optical transmission through rain," *Appl. Opt.*, vol. 35, no. 36, p. 7144, Dec. 1996.

[24] A. A. Kokhanovsky and A. Macke, "Integral light-scattering and absorption characteristics of large, nonspherical particles," *Appl. Opt.*, vol. 36, no. 33, p. 8785, Nov. 1997.

[25] A. Macke and M. Großklaus, "Light scattering by nonspherical raindrops," *J. Quant. Spectrosc. Radiat. Transf.*, vol. 60, no. 3, pp. 355–363, Sep. 1998.

[26] G. Roy and L. R. Bissonnette, "Strong dependence of rain-induced lidar depolarization on the illumination angle: Experimental evidence and geometrical-optics interpretation," *Appl. Opt.*, vol. 40, no. 27, p. 4770, Sep. 2001.

[27] P. A. Lewandowski, W. E. Eichinger, A. Kruger, and W. F. Krajewski, "Lidar-based estimation of small-scale rainfall: Empirical evidence," *J. Atmos. Ocean. Technol.*, vol. 26, no. 3, pp. 656–664, Mar. 2009.

[28] G. J. Kunz and G. de Leeuw, "Inversion of lidar signals with the slope method," *Appl. Opt.*, vol. 32, no. 18, p. 3249, Jun. 1993.

[29] E. N. Rasmussen and S. Koch, "VORTEX-SE: Lessons learned and early results," in *Proc. 28th Conf. Severe Local Storms*, 2016. [Online]. Available: https://ams.confex.com/ams/28SLS/webprogram/Paper301782.html

[30] D. T. Dawson et al., "Overview of purdue's mobile disdrometer operations during VORTEX-SE," in *Proc. 28th Conf. Severe Local Storms*, 2016, p. 16A.2. [Online]. Available: https://ams.confex.com/ams/28SLS/webprogram/Paper301887.html

[31] *User's Guide Vaisala Ceilometer CL51*, Vaisala, Vantaa, Finland, 2010.

[32] E. J. O'Connor, A. J. Illingworth, and R. J. Hogan, "A technique for autocalibration of cloud lidar," *J. Atmos. Ocean. Technol.*, vol. 21, no. 5, pp. 777–786, May 2004.

[33] T. Ince, S. J. Frasier, A. Muschinski, and A. L. Pazmany, "An S-band frequency-modulated continuous-wave boundary layer profiler: Description and initial results," *Radio Sci.*, vol. 38, no. 4, p. 1072, Aug. 2003.

[34] E. E. Gossard, "Radar research on the atmospheric boundary layer," in *Proc. Radar Meteorology: Battan Memorial 40th Anniversary Radar Meteorol. Conf.*, D. Atlas, Ed. Boston, MA, USA: American Meteorological Society, 1990, pp. 477–527.

[35] F. Martin Ralph, "Using radar-measured radial vertical velocities to distinguish precipitation scattering from clear-air scattering," *J. Atmos. Ocean. Technol.*, vol. 12, no. 2, pp. 257–267, Apr. 1995.

[36] B. E. Martner, S. E. Yuter, A. B. White, S. Y. Matrosov, D. E. Kingsmill, and F. M. Ralph, "Raindrop size distributions and rain characteristics in California coastal rainfall for periods with and without a radar bright band," *J. Hydrometeorol.*, vol. 9, no. 3, pp. 408–425, Jun. 2008.

[37] X. Lin and A. Y. Hou, "Estimation of rain intensity spectra over the continental United States using ground radar–gauge measurements," *J. Climate*, vol. 25, no. 6, pp. 1901–1915, Mar. 2012.

[38] *Operating Instructions—Present Weather Sensor Parsivel*, OTT, Kuthambakkam, India, 2004.

[39] A. Tokay, D. B. Wolff, and W. A. Petersen, "Evaluation of the new version of the laser-optical disdrometer, OTT Parsivel2," *J. Atmos. Ocean. Technol.*, vol. 31, no. 6, pp. 1276–1288, Jun. 2014.

[40] Leosphere. (2017). *Windcube 100S/200S/400S*. Accessed: Nov. 17, 2017. [Online]. Available: http://www.leosphere.com/products/3d-scanning/windcube-100s200s400s-turbulence-wind-lidar

[41] K. A. Browning and R. Wexler, "The determination of kinematic properties of a wind field using Doppler radar," *J. Appl. Meteorol.*, vol. 7, no. 1, pp. 105–113, Feb. 1968.

[42] S. W. Henderson, P. Gatt, D. Rees, and M. Huffaker, "Wind Lidar," in *Laser Remote Sensing*, T. Fujii and T. Fukuchi, Eds. Boca Raton, FL, USA: CRC Press, 2005, p. 912.

[43] J. G. Proakis and D. G. Manolakis, "Design of digital filters," in *Digital Signal Processing. Principles, Algorithms and Applications*, 4th ed. London, U.K.: Pearson, 2007, pp. 654–749.

[44] F. Rocadenbosch, A. Comerón, and D. Pineda, "Assessment of lidar inversion errors for homogeneous atmospheres," *Appl. Opt.*, vol. 37, no. 12, p. 2199, Apr. 1998.

[45] M. N. Md Reba, F. Rocadenbosch, M. Sicard, C. Munoz, and S. Tomas, "Piece-wise variance method for signal-to-noise ratio estimation in elastic/Raman lidar signals," in *Proc. IEEE Int. Geosci. Remote Sens. Symp.*, Jul. 2007, pp. 3158–3161.

[46] C. R. Williams, "Vertical air motion retrieved from dual-frequency profiler observations," *J. Atmos. Ocean. Technol.*, vol. 29, no. 10, pp. 1471–1480, Oct. 2012.

[47] B. E. Vieux and P. B. Bedient, "Estimation of rainfall for flood prediction from WSR-88D reflectivity: A case study, 17–18 October 1994*," *Weather Forecasting*, vol. 13, no. 2, pp. 407–415, Jun. 1998.

[48] J. D. Klett, "Lidar calibration and extinction coefficients," *Appl. Opt.*, vol. 22, no. 4, p. 514, Feb. 1983.

[49] J. D. Klett, "Stable analytical inversion solution for processing lidar returns," *Appl. Opt.*, vol. 20, no. 2, p. 211, Jan. 1981.

[50] F. G. Fernald, "Analysis of atmospheric lidar observations: Some comments," *Appl. Opt.*, vol. 23, no. 5, p. 652, Mar. 1984.

[51] V. A. Kovalev and W. E. Eichinger, "Analytical Solutions of the Lidar equation," in *Elastic Lidar. Theory, Practice, and Analysis Methods*. Hoboken, NJ, USA: Wiley, 2004, pp. 105–142.

[52] G. J. Kunz, "Remote sensing of the propagation environment," in *Proc. AGARD Conf.*, 1992, pp. 1–11.

[53] F. Fabry and I. Zawadzki, "Long-term radar observations of the melting layer of precipitation and their interpretation," *J. Atmos. Sci.*, vol. 52, no. 7, pp. 838–851, Apr. 1995.

[54] D. York, N. M. Evensen, M. L. Martínez, and J. De Basabe Delgado, "Unified equations for the slope, intercept, and standard errors of the best straight line," *Amer. J. Phys.*, vol. 72, no. 3, pp. 367–375, Mar. 2004.

[55] H. Sauvageot, "The probability density function of rain rate and the estimation of rainfall by area integrals," *J. Appl. Meteorol.*, vol. 33, no. 11, pp. 1255–1262, Nov. 1994.

[56] R. J. Barlow, "Theoretical distributions," in *Statistics: A Guide to the Use of Statistical Methods in the Physical Sciences*, D. J. Sandiford, F. Mandl, A. C. Phillips, Eds. Chichester, U.K.: Wiley, 1989, pp. 48–67.

[57] C. McNicholas and D. D. Turner, "Characterizing the convective boundary layer turbulence with a high spectral resolution lidar," *J. Geophys. Res., Atmos.*, vol. 119, no. 22, pp. 12910–12927, Nov. 2014.

[58] C. A. Cantrell, "Technical note: Review of methods for linear least-squares fitting of data and application to atmospheric chemistry problems," *Atmos. Chem. Phys.*, vol. 8, no. 17, pp. 5477–5487, 2008.

[59] *MRR Physical Basics*, METEK Meteorologische Messtechnik GmbH, Elmshorn, Germany, 2009.

[60] J. S. Marshall, W. Hitschfeld, and K. L. S. Gunn, "Advances in radar weather," *Adv. Geophys.*, vol. 2, pp. 1–56, Jan. 1955.

[61] R. S. Sekhon and R. C. Srivastava, "Doppler radar observations of drop-size distributions in a thunderstorm," *J. Atmos. Sci.*, vol. 28, no. 6, pp. 983–994, Sep. 1971.

[62] P. T. Willis and P. Tattelman, "Drop-size distributions associated with intense rainfall," *J. Appl. Meteorol.*, vol. 28, no. 1, pp. 3–15, Jan. 1989.

[63] A. Tokay and D. A. Short, "Evidence from tropical raindrop spectra of the origin of rain from stratiform versus convective clouds," *J. Appl. Meteorol.*, vol. 35, no. 3, pp. 355–371, Mar. 1996.

[64] L. J. Battan, *Radar Observations of the Atmosphere*. Chicago, IL, USA: Univ. of Chicago Press, 1973.

[65] R. Gunn and G. D. Kinzer, "The terminal velocity of fall for water droplets in stagnant air," *J. Meteorol.*, vol. 6, no. 4, pp. 243–248, Aug. 1949.

[66] D. Atlas, R. C. Srivastava, and R. S. Sekhon, "Doppler radar characteristics of precipitation at vertical incidence," *Rev. Geophys.*, vol. 11, no. 1, p. 1, 1973.

[67] G. B. Foote and P. S. Du Toit, "Terminal velocity of raindrops aloft," *J. Appl. Meteorol.*, vol. 8, no. 2, pp. 249–253, Apr. 1969.

[68] A. Tokay, P. Hartmann, A. Battaglia, K. S. Gage, W. L. Clark, and C. R. Williams, "A field study of reflectivity and Z–R relations using vertically pointing radars and disdrometers," *J. Atmos. Ocean. Technol.*, vol. 26, no. 6, pp. 1120–1134, Jun. 2009.

Francesc Rocadenbosch (Senior Member, IEEE) received the B.S. and Ph.D. degrees in telecommunications engineering from the Universitat Politècnica de Catalunya (UPC), Barcelona, Spain, in 1991 and 1996, respectively, and the M.B.A. degree from the University of Barcelona, Barcelona, in 2001.

In 1993, he joined the Department of Signal Theory and Communications, UPC, where he is a Full Professor. Since 1996, he has steered the development of CommSensLab-UPC Excellence-Unit activities on lidar, including the UPC unmanned lidar station (ESFRI 2016 roadmap), and he has served on over ten collaborative remote sensing projects as PI. His research interests include remote sensing (lidar-radar-radiometry) for atmospheric observation, related signal processing, and off-shore wind lidar.

Dr. Rocadenbosch was a recipient of the "Salvà i Campillo" Best Research Project Award in 1997, the National Telecom Award in 2003 (group), and the EU KIC recognition for EOLOS spin-off in 2015. He is an Associate Editor of the IEEE TRANSACTIONS ON GEOSCIENCE AND REMOTE SENSING.

Rubén Barragán received the B.S. degree in environmental sciences from Rey Juan Carlos University, Madrid, Spain, in 2010, and the M.S. degree in remote sensing from the University of Alcalá de Henares, Madrid, in 2011. He is pursuing the Ph.D. degree in telecommunications engineering with the Universitat Politècnica de Catalunya, Barcelona, Spain.

His research interests include multispectral lidar signal processing, radiative forcing estimation, and characterization of precipitation by means of remote sensing techniques.

Stephen J. Frasier (Senior Member, IEEE) received the B.E.E. degree from the University of Delaware, Newark, DE, USA, in 1987, and the Ph.D. degree from the University of Massachusetts, Amherst, MA, USA, in 1994.

From 1987 to 1990, he was with SciTec, Inc., Princeton, NJ, USA (a subsidiary of TRW), analyzing the electromagnetic and optical signatures of rocket plumes, evaluating laser detection systems, and developing data acquisition systems supporting airborne IR sensors. From 1994 to 1997, he was employed by the University of Massachusetts, as a Research Engineer and a Senior Research Fellow, where he is a Professor and the Co-Director of Microwave Remote Sensing Laboratory, Department of Electrical and Computer Engineering. In 2005, he spent a sabbatical year with the Electromagnetic and Photonics Engineering Group, Polytechnic University of Catalonia (UPC), Barcelona, Spain, and in 2012 with the Center for Radar Meteorology - Météo France, Toulouse, France. He has served as the Co-Chair of the Airborne Phased Array Radar Advisory Panel for the National Center for Atmospheric Research (NCAR), Boulder, CO, USA. He leads research programs in phased-array polarimetry for meteorological applications and in the measurement of surface winds over the oceans. His research interests include microwave imaging and interferometric techniques, radar oceanography, and radar meteorology.

Dr. Frasier is a member of the IEEE Geoscience and Remote Sensing Society, the URSI Commission F, the American Geophysical Union, and the American Meteorological Society.

Joseph Waldinger received the B.S.E.E. degree from the New Jersey Institute of Technology, Newark, NJ, USA, in 2015, and the M.S. degree in electrical and computer engineering from the University of Massachusetts, Amherst, MA, USA, in 2018.

From 2015 to 2018, he was a Research Assistant with the Microwave Remote Sensing Laboratory, University of Massachusetts, where his graduate study focused on atmospheric boundary layer profiling via frequency-modulated continuous-wave radar. He is with Mercury Systems, Caldwell, NJ, USA.

David D. Turner received the B.A. and M.S. degrees in mathematics from Eastern Washington University, Cheney, WA, USA, in 1992 and 1994, respectively, and the Ph.D. degree in atmospheric science from the University of Wisconsin—Madison, Madison, WI, USA, in 2003.

He is a Physical Meteorologist with the Global Systems Division, Earth System Research Laboratory, National Oceanic and Atmospheric Administration (NOAA), Boulder, CO, USA. His research interests include infrared and microwave remote sensing, radiative transfer in clear and cloudy atmospheres, water vapor and wind profiling lidar technologies, retrieval theory, and using these observations to improve our ability to model the evolution of the atmospheric boundary layer over the diurnal cycle during dynamic weather events.

Dr. Turner is a member of the American Meteorological Society and the American Geophysical Union.

Robin L. Tanamachi received the B.S. degree in atmospheric and oceanic sciences from the University of Wisconsin—Madison, Madison, WI, USA, in 2001, and the M.S. and Ph.D. degrees in meteorology from The University of Oklahoma, Norman, OK, USA, in 2004 and 2011, respectively.

She is an Assistant Professor with the Department of Earth, Atmospheric, and Planetary Sciences, Purdue University, West Lafayette, IN, USA. Her interests include radar meteorology, severe thunderstorm dynamics and kinematics, and methods for assimilating radar observations into numerical weather prediction models.

Dr. Tanamachi is a member of the American Meteorological Society (AMS) and served on the AMS Radar Meteorology Committee from 2013 to 2019.

Daniel T. Dawson, II received the B.S. degree in atmospheric dynamics from Purdue University, West Lafayette, IN, USA, in 2002, and the M.S. and Ph.D. degrees in meteorology from The University of Oklahoma, Norman, OK, USA, in 2004 and 2009, respectively.

He is an Assistant Professor with the Department of Earth, Atmospheric, and Planetary Sciences, Purdue University. His research interests include the microphysics and dynamics of severe convective storms and tornadoes, rain drop size distributions in convective storms, storm-scale numerical weather prediction, and radar data assimilation techniques.

Dr. Dawson, II is a member of the American Meteorological Society and serves on the Verification of the Origins of Rotation in Tornadoes Experiment Southeast (VORTEX-SE) Scientific Steering Committee (SSC) and the Planning Committee for the upcoming Non-Classic Tornadic Storms (NCTS) Field Program.